Simulating the unsteady stable boundary layer with a stochastic stability equation

Nikki Vercauteren[1] and Vyacheslav Boyko[2]

[1]University of Oslo
[2]Freie Universität Berlin

June 7, 2023

Abstract

Turbulence in stable boundary layers is typically unsteady and intermittent. The study implements a stochastic modelling approach to represent unsteady mixing possibly associated with intermittency of turbulence and with unresolved fluid motions such as dirty waves or drainage flows. The stochastic parameterization is introduced by randomizing the mixing lengthscale used in a Reynolds average Navier-Stokes (RANS) model with turbulent kinetic energy closure, resulting in a stochastic unsteady RANS model. The randomization alters the turbulent momentum diffusion and accounts for sporadic events of possibly unknown origin that cause unsteady mixing. The paper shows how the proposed stochastic parameterization can be integrated into a RANS model used in weather-forecasting and its impact is analyzed using neutrally and stably stratified idealized numerical case studies. The simulations show that the framework can successfully model intermittent mixing in stably stratified conditions, and does not alter the representation of neutrally stratified conditions. It could thus present a way forward for dealing with the complexities of unsteady flows in numerical weather prediction or climate models.

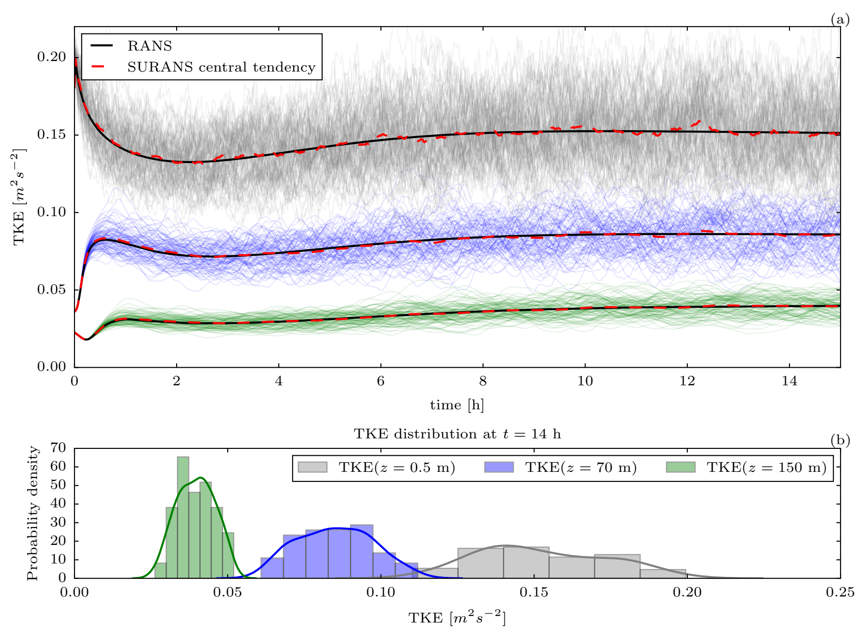

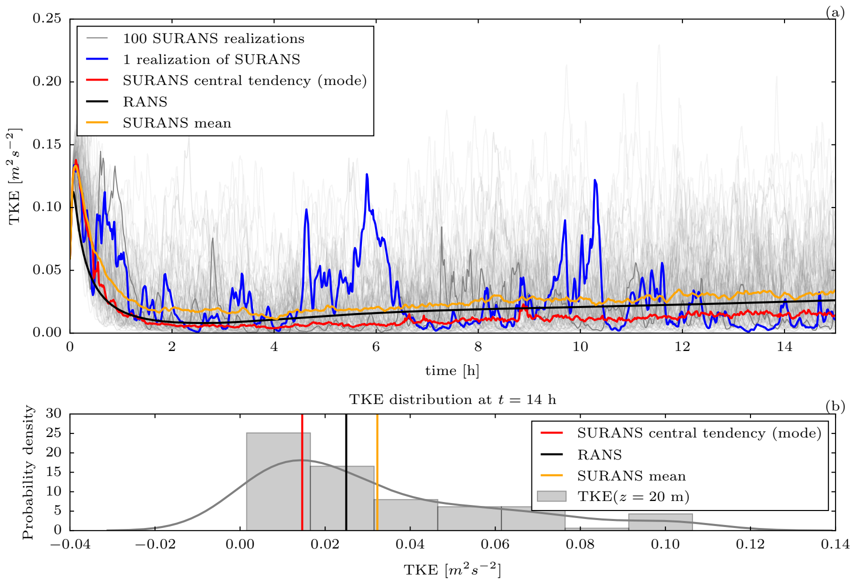

(a)
100 SURANS realizations
1 realization of SURANS
SURANS central tendency (mode)
RANS
SURANS mean
TKE $[m^2 s^{-2}]$
time [h]
TKE distribution at $t = 14$ h
(b)
Probability density
SURANS central tendency (mode)
RANS
SURANS mean
TKE($z = 20$ m)
TKE $[m^2 s^{-2}]$

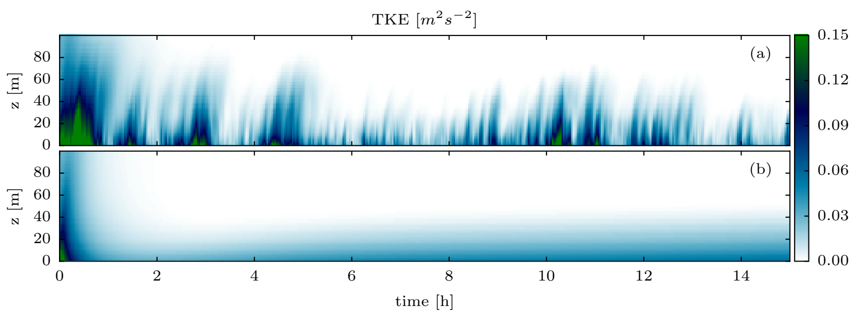

TKE $[m^2 s^{-2}]$
(a)
(b)
z [m]
time [h]

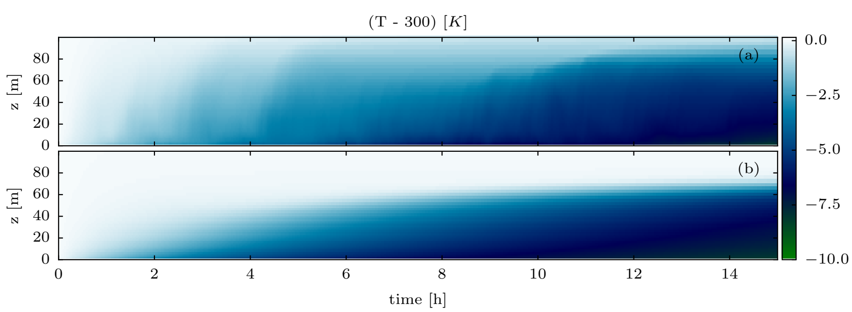

(T - 300) $[K]$
(a)
(b)
z [m]
time [h]

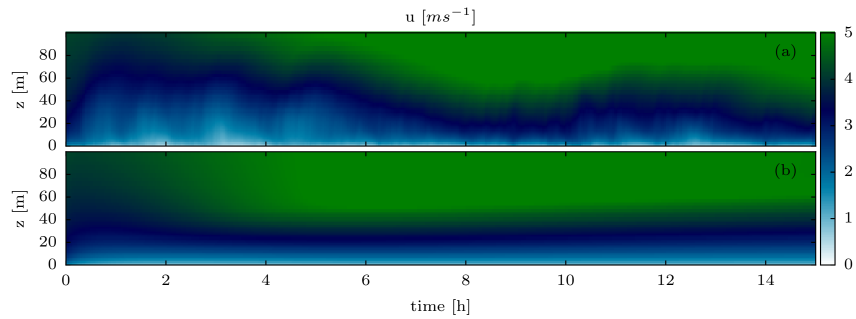
u [ms^{-1}]
(a)
(b)
z [m]
time [h]

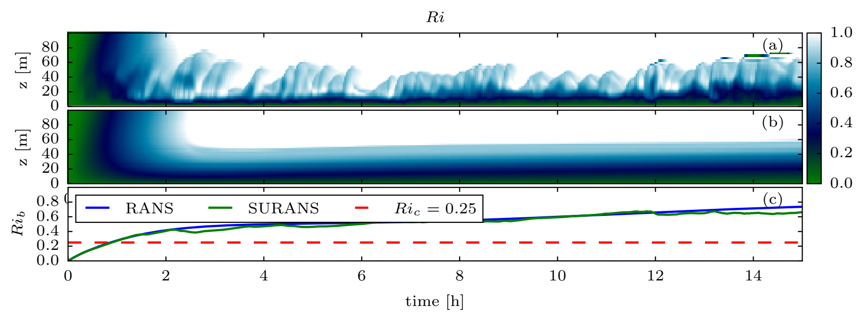
Ri
(a)
(b)
(c)
z [m]
Ri_b
RANS
SURANS
$Ri_c = 0.25$
time [h]

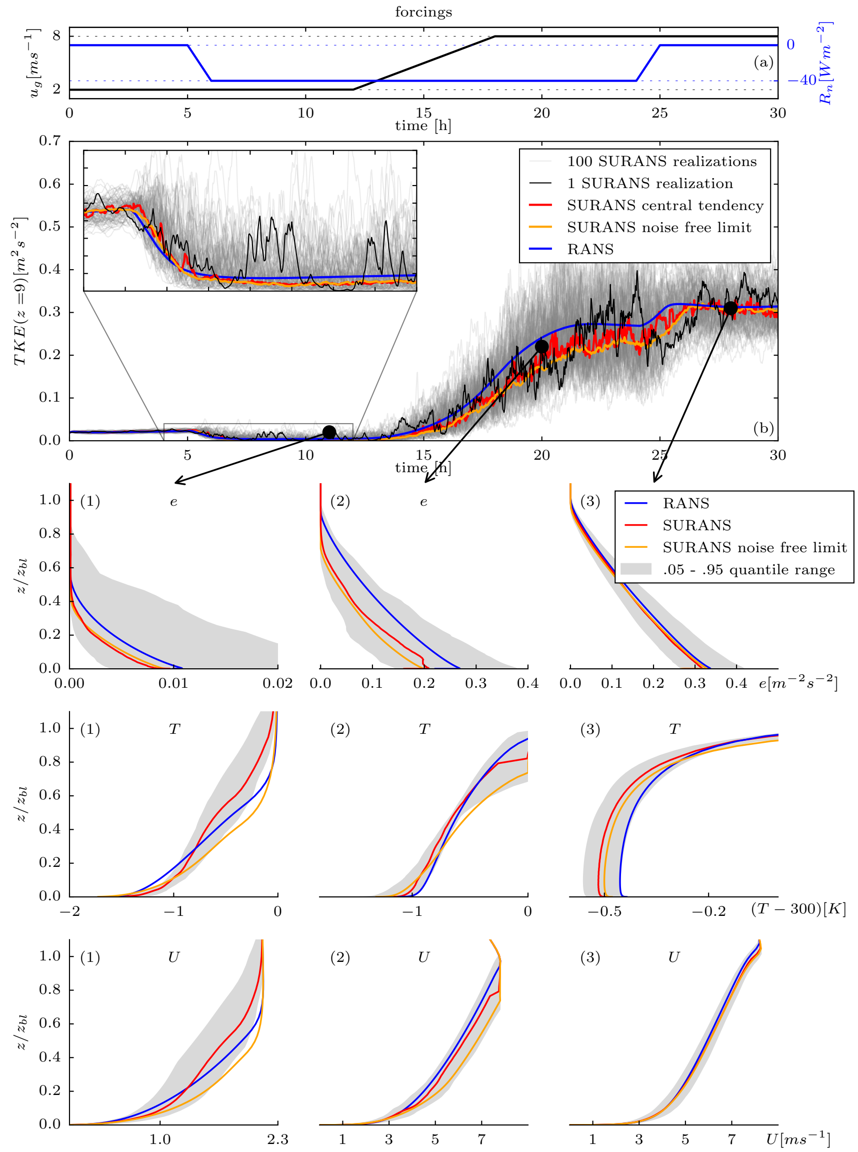
forcings
(a)
(b)
time [h]
100 SURANS realizations
1 SURANS realization
SURANS central tendency
SURANS noise free limit
RANS
SURANS
.05 - .95 quantile range
(1)
(2)
(3)

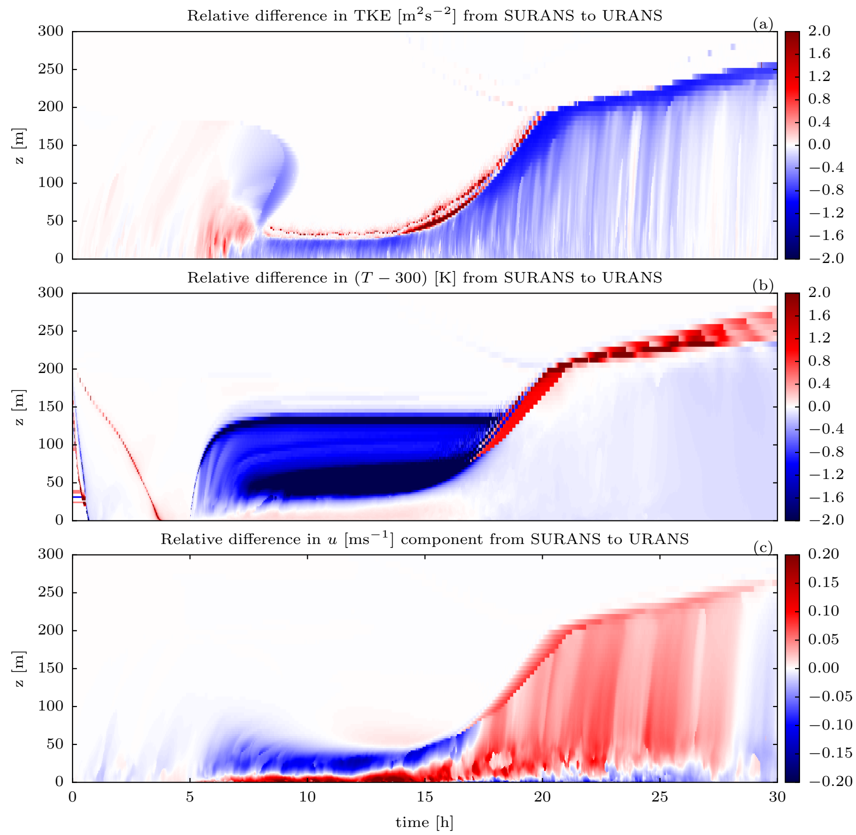
Relative difference in TKE [m^{2}s^{-2}] from SURANS to URANS
(a)
Relative difference in $(T - 300)$ [K] from SURANS to URANS
(b)
Relative difference in u [ms^{-1}] component from SURANS to URANS
(c)
z [m]
time [h]

Simulating the unsteady stable boundary layer with a stochastic stability equation

Vyacheslav Boyko[1] **and Nikki Vercauteren**[2,3]

[1]Department of Mathematics and Computer Sciences, Freie Universität Berlin, Berlin, Germany
[2]Department of Geosciences, University of Oslo, Oslo, Norway
[3]Institute for Geophysics and Meteorology, University of Cologne, Cologne, Germany

Key Points:

- A stochastic parameterization of turbulence is implemented in a Reynolds average Navier-Stokes (RANS) model to represent unsteady mixing.
- The introduced stochastic perturbations of the mixing length enable the simulation of intermittent turbulence in the stable boundary layer.
- The stochastic unsteady RANS model does not alter the simulation of neutral conditions.

Corresponding author: Nikki Vercauteren, `Nikki.Vercauteren@geo.uio.no`

Abstract

Turbulence in stable boundary layers is typically unsteady and intermittent. The study implements a stochastic modelling approach to represent unsteady mixing possibly associated with intermittency of turbulence and with unresolved fluid motions such as dirty waves or drainage flows. The stochastic parameterization is introduced by randomizing the mixing lengthscale used in a Reynolds average Navier-Stokes (RANS) model with turbulent kinetic energy closure, resulting in a stochastic unsteady RANS model. The randomization alters the turbulent momentum diffusion and accounts for sporadic events of possibly unknown origin that cause unsteady mixing. The paper shows how the proposed stochastic parameterization can be integrated into a RANS model used in weather-forecasting and its impact is analyzed using neutrally and stably stratified idealized numerical case studies. The simulations show that the framework can successfully model intermittent mixing in stably stratified conditions, and does not alter the representation of neutrally stratified conditions. It could thus present a way forward for dealing with the complexities of unsteady flows in numerical weather prediction or climate models.

Plain Language Summary

Limited computer resources lead to a simplified representation of unresolved small-scale processes in weather forecasting and climate models, through parameterization schemes. Among the parameterised processes, turbulent fluxes exert a critical impact on the exchange of heat, water and carbon between the land and the atmosphere. Turbulence theory was, however, developed for homogeneous and flat terrain, with stationary conditions. At nighttime or in cold environment, turbulence is typically non-stationary, weak and intermittent and the classical theory fails. Part of the intermittent mixing is due to turbulence enhancement by small-scale wind variability. In the following, a random modelling approach is used to enhance turbulent mixing due to small-scale wind variability and intermittency of mixing. The proposed approach is shown to be a viable approach to represent the effect of small-scale variability of mixing for different atmospheric flow conditions.

1 Introduction

The representation of the atmospheric boundary layer in stably stratified conditions is an intricate problem for numerical weather prediction (NWP) and climate models (Holtslag et al., 2013; Sandu et al., 2013). Stably stratified conditions can occur at nighttime when radiative cooling of the surface is predominant, or when warm air is advected over a cold surface, for example over snow or ice. Such conditions favour model biases, a prominent example being systematic errors in the near-surface temperature (Davy & Esau, 2014; Esau et al., 2018; Køltzow et al., 2019). The different processes occurring at the interface between the surface and the lower atmosphere interact in complex ways, making the identification of the main source of error challenging. Model errors have been related to shortcomings in the calculation of turbulent fluxes, radiative fluxes or ground heat fluxes, as well as to an overestimated heat capacity of a too deep boundary layer, preventing a sufficiently fast reaction of the near-surface temperature (Tjernström et al., 2005; Sandu et al., 2013; Esau et al., 2018).

Turbulence in the stable boundary layer (SBL) is generated by shear production, while its development is inhibited by buoyant forces. Due to this interplay, flow regimes with different physical and dynamical characteristics exist (van de Wiel & Moene, 2003; Mahrt, 2014). Fully turbulent SBL, also coined as weakly stable boundary layers, are rather well described by similarity theory, but the very stable boundary layer with intermittent turbulence is less well understood (Grachev et al., 2005; Mahrt, 2014; LeMone et al., 2018). At high stability, non-turbulent processes become more important, and the flow is characterised by strong non-stationarity (Mahrt & Bou-Zeid, 2020). For example, larger scale wave-like motions can interact in complex ways and contribute to intermittent turbulence (Cava et al., 2019). Non-turbulent flow features smaller than those traditionally classified as mesoscales, denoted as submesoscale motions, exist under all atmospheric stratifications for weak winds (Anfossi et al., 2005), but exert a critical influence under strong stratification. In these conditions characterised by a large Richardson number, turbulence production is closely related to local short-term accelerations associated with submeso motions (Mahrt, 2011; Boyko & Vercauteren, 2020; Lan et al., 2022). Approaches to parameterise non-turbulent motions are being developed, including the quasi-normal scale elimination (QNSE, Sukoriansky et al. (2005)) that includes breaking gravity waves, or a quantification of wave drag due to small scale orography (Steeneveld et al., 2009). Another closure approach is based on the total turbulent energy that considers the potential energy due to density fluctuations of the fluid in addition to the traditional consideration of turbulent kinetic energy (Zilitinkevich et al., 2007; Mauritsen et al., 2007). A unified treatment of non-stationary turbulence in very stable conditions is however lacking (LeMone et al., 2018; Edwards et al., 2020).

With weak winds and clear-sky conditions, associated with strong stability, the atmosphere may become decoupled from the surface (Acevedo et al., 2016). This occurs when a layer near the surface becomes driven by radiation and soil thermal transport, while the surface turbulent heat flux is too weak to sustain the energy demand of the surface (Van de Wiel et al., 2012). In NWP, the decoupling can occur in very localised regions with a high spatial variability, and the positive feedback between weakening turbulence and radiative cooling can lead to further rapid cooling in decoupled regions (Kähnert et al., 2022). To avoid such decoupling and so-called runaway cooling to become unphysically important in models, operational parameterisation schemes have implemented rather high levels of turbulent mixing (Louis, 1979; Derbyshire, 1999; Cuxart et al., 2006). This practice is often justified by the need to account for the numerous processes impacting mixing that are not resolved in NWP and climate models, such as unresolved surface heterogeneity or topography, and internal gravity waves. This enhancement of turbulent mixing is typically calibrated to reduce the activity of synoptic systems and improve model scores, with the negative consequence that NWP and climate models simulate too deep boundary layers, too weak low-level jets or wind veering with height (Sandu et al., 2013).

In an effort to model the variability of mixing related to intermittency of turbulence, internal or related to submeso motions, Boyko and Vercauteren (n.d.) devised a stochastic extension to Monin–Obukhov Similarity Theory (MOST) that is able to model intermittent turbulent bursts. The proposed approach keeps the physical basis of MOST untouched, assuming a gradient-diffusion model in which the diffusivity scales with an appropriate lengthscale incorporating the influence of dimensionless stability. It extends MOST by treating the stability correction and thus the mixing lengthscale as a time-continuous stochastic variable, thereby enabling the representation of unsteady mixing. There may be intrinsic limits in such a gradient-diffusion model structure, even when the diffusion coefficient is stochastic, however turbulence parameterisation schemes used in operational NWP models were shown to reasonably capture the physics of the SBLs for a variety of forcing provided they do not apply excessive vertical mixing (Cuxart et al., 2006; Baas et al., 2018, 2019). Using tools from uncertainty quantification, Audouin et al. (2021) concluded that model deficiencies reflect a poor parameterization calibration rather than intrinsic limits of the parameterization formulation. These authors further suggested a framework combining single-column models and large eddy simulations to improve the calibration of SBL model parameters. In the observational study presented in Boyko and Vercauteren (n.d.), the calibration of a proposed time continuous stochastic stability equation is analysed statistically using field observations and inverse modelling methods. The results highlight scaling of the stochastic model parameters with dimensionless atmospheric stability, providing a closed-form parametrisation of turbulence that enables explicit treatment of the uncertainty of the fluxes to be modelled. Due to the time-continuous model structure, the proposed stochastic extension of MOST enables the representation of localised bursts of turbulence through a stochastic model. Such a stochastic parameterisation of turbulence can provide much needed uncertainty estimations, and may also be needed to better represent the mean state and SBL regime transitions that can occur via inherent nonlinear processes (Berner et al., 2017; Van de Wiel et al., 2017).

In this study, the stochastic representation of the mixing length is implemented into a Reynolds-averaged Navier–Stokes (RANS) model. The momentum and heat diffusivity, as well as all the state variables are predicted from a stochastic mixing length according to the stochastic stability equation introduced by Boyko and Vercauteren (n.d.). The fact that stochastic perturbations are introduced enables intermittency to be modeled. The study investigates the impact of the suggested stochastic scheme on a range of numerical case studies to evaluate the robustness of the proposed framework. The stochastic model, coined as Stochastically Unsteady Reynolds-averaged Navier–Stokes Equations (SURANS), is presented in section 2 and its numerical implementation in introduced in section 3. Section 4 presents the results of numerical case studies, which include a neutrally stratified boundary layer, a stably stratified boundary layer, followed by a case with variable geostrophic wind and radiative forcing. A summary and conclusions are given in section 5.

2 A Stochastic Model of the Unsteady Stable Boundary Layer

2.1 Deterministic model

For a flat surface in a dry atmosphere, assuming horizontal homogeneity, neglecting radiative flux divergence, applying the Boussinesq approximation, and using a turbulence closure model based on eddy diffusivities (where $\overline{w'u'} = -K_m \frac{\partial u}{\partial z}$, $\overline{w'v'} = -K_m \frac{\partial v}{\partial z}$, and $\overline{w'\theta'} = -K_h \frac{\partial \theta}{\partial z}$), the idealised Stable Boundary Layer (SBL) can be represented by the following RANS model (Stull, 1988):

$$\frac{\partial u}{\partial t} = (v - v_g) f_c + \frac{\partial}{\partial z}\left(K_m \frac{\partial u}{\partial z}\right) \tag{1}$$

$$\frac{\partial v}{\partial t} = -(u - u_g) f_c + \frac{\partial}{\partial z}\left(K_m \frac{\partial v}{\partial z}\right) \tag{2}$$

$$\frac{\partial \theta}{\partial t} = \frac{\partial}{\partial z}\left(K_h \frac{\partial \theta}{\partial z}\right) \tag{3}$$

$$\frac{\mathrm{d}\theta_g}{\mathrm{d}t} = \frac{1}{C_g}(R_n - H_0) - \kappa_m(\theta_g - \theta_s) \tag{4}$$

where u, v are the mean (Reynolds averaged) horizontal wind components and θ is the mean potential temperature. The horizontal pressure gradient is prescribed through the geostrophic velocity above the SBL, whose wind components are (u_g, v_g), and f_c is the Coriolis parameter. The ground surface temperature θ_g is the bottom boundary condition of Eq. (3) and its evolution is modeled using a force-restore method (Stull, 1988; Garratt, 1994; Acevedo et al., 2021). The thermal capacity of the soil per unit area is denoted with C_g. The soil heat transfer coefficient $\kappa_m = 1.18\omega$ is related to the Earth's angular frequency ω. $H_0 = \rho c_p \overline{w'\theta'}_0$ is the surface sensible heat flux, where ρ is the air density and c_p is the specific heat of air at constant pressure, and R_n is the net radiation. The temperature below the surface θ_s at some finite depth is nearly constant and fluctuates on a seasonal scale. It is, therefore, deemed fixed for the simulation of individual nights.

Closing the model requires further specification of the eddy diffusivities K_m and K_h. Many operational NWP schemes use first-order schemes, in which the eddy diffusivity depends on the wind speed, a specified mixing lengthscale and a stability function (Cuxart et al., 2006). Higher-order schemes add more prognostic equations to the model to compute turbulent quantities. A common choice is that of a 1.5 order closure, in which a prognostic equation is used only for the evolution of the Turbulence Kinetic Energy (TKE), e. In this case, which will be further developed in the following model extension, the eddy diffusivity for momentum is expressed as follow:

$$K_m = \alpha l_m \sqrt{e} \tag{5}$$

$$\frac{\partial e}{\partial t} = P_e + \frac{\partial}{\partial z}\left(K_m \frac{\partial e}{\partial z}\right) - \epsilon, \tag{6}$$

$$\tag{7}$$

where l_m stands for the momentum mixing length and α is a modelling constant (Cuxart et al., 2006; Rodrigo & Anderson, 2013). In the evolution equation for e, Eq. (6), P_E represents the production of TKE and ϵ its dissipation rate. Turbulent kinetic energy is produced through wind shear and buoyancy, hence

$$P_e = -\overline{u'w'}\frac{\partial u}{\partial z} - \overline{v'w'}\frac{\partial v}{\partial z} + \frac{g}{\Theta_0}\overline{w'\theta'} = K_m\left[\left(\frac{\partial u}{\partial z}\right)^2 + \left(\frac{\partial v}{\partial z}\right)^2\right] - \frac{g}{\Theta_0}K_h\frac{\partial \theta}{\partial z}. \tag{8}$$

where $g = 9.81$ m s^{-2} is the gravitational acceleration, $\Theta_0 = 300$ K is a reference potential temperature. The dissipation rate ϵ is modelled using a dissipation length l_ϵ, which is assumed equal to the mixing length in our study, i.e. $l_\epsilon = l_m$, leading to

$$\epsilon = \frac{(\alpha_\varepsilon e)^{3/2}}{l_m} \tag{9}$$

where α_ε is a modelling constant set to $\alpha_\varepsilon = 0.1$ in this study (Cuxart et al., 2006; Rodrigo & Anderson, 2013). The turbulent Prandtl number $Pr_t = \frac{K_m}{K_h}$ can be used to obtain K_h from K_m and in the following, it is set to one for simplicity. A detailed presentation of several operational 1.5 order schemes can be found in Cuxart et al. (2006), where it can be seen that schemes differ in the values selected for the constants, in the parameterisation used for the mixing lengths and in the stability functions used to scale the eddy diffusivities according to the static stability.

2.2 Stochastic Extension

The model extension implemented in this work, denoted as SURANS model, is developed as a set of prognostic equations for simulating unsteady intermittent turbulent mixing in the SBL. The main difference to the RANS model is a stochastic extension of MOST in the form of a Stochastic Stability Equation (SSE) representing the evolution of a stability correction variable. The SSE derives from a data-driven modelling approach introduced by Boyko and Vercauteren (n.d.) with the goal of modelling the variability of turbulent fluxes due to the influence of unresolved submesoscale motions and more generally to turbulence intermittency. The SSE is limited at this stage of research to the near-surface boundary layer where field observations were analysed, and hence the following numerical implementation is meant to serve as a proof-of-concept where the effect of intermittent mixing is modeled to a certain maximum height above the surface. The impact of such a modelling strategy is analysed based on selected numerical case studies. The height-limited implementation is chosen because the SSE was calibrated based on measurements up to 30 m at one field site (Boyko & Vercauteren, n.d.). The set of equations forming the SURANS model complements the model (1)–(6) as follows:

$$\frac{\partial u}{\partial t} = (v - v_g) f_c + \frac{\partial}{\partial z}\left(K_m(\phi)\frac{\partial u}{\partial z}\right) - N_u \tag{10}$$

$$\frac{\partial v}{\partial t} = -(u - u_g) f_c + \frac{\partial}{\partial z}\left(K_m(\phi)\frac{\partial v}{\partial z}\right) - N_v \tag{11}$$

$$\frac{\partial \theta}{\partial t} = \frac{\partial}{\partial z}\left(K_h(\phi)\frac{\partial \theta}{\partial z}\right) \tag{12}$$

$$\frac{\partial e}{\partial t} = \frac{\partial}{\partial z}\left(K_m(\phi)\frac{\partial e}{\partial z}\right) + K_m(\phi)\left[\left(\frac{\partial u}{\partial z}\right)^2 + \left(\frac{\partial v}{\partial z}\right)^2\right] - \frac{g}{\Theta_0}K_h(\phi)\frac{\partial \theta}{\partial z} - \frac{(\alpha_\varepsilon e)^{3/2}}{l_m(\phi)} \tag{13}$$

$$\frac{\mathrm{d}\theta_g}{\mathrm{d}t} = \frac{1}{C_g}(R_n - H_0) - \kappa_m(\theta_g - \theta_s) \tag{14}$$

$$d\phi = \tau_h^{-1}(1 + \Lambda(Ri)\phi - \mathcal{V}(Ri)\phi^2)dt + \tau_h^{-1/2}\Sigma(Ri)\phi\, dW_t \tag{15}$$

The SSE as equation (15) is the novel contribution to the classical RANS model and implements a time varying stochastic stability correction variable ϕ introduced in Boyko and Vercauteren (n.d.) and which will be discussed further below. Relaxation terms $N_u = (u - u_g)/\tau_r$ and $N_v = (v - v_g)/\tau_r$ are added to the momentum equations in (10) and (11), where τ_r is the relaxation time. Those nudge the solution towards the geostrophic wind and are used to damp inertial oscillations that become too important when turbulent mixing is weak, which is likely unphysical. The value of τ_r is set in a range of 3–6 hours, such that the solution is largely controlled by (10)-(15) and only mildly nudged towards the geostrophic forcing (u_g, v_g). The prognostic Eq. (13) describes the evolution of the TKE according to the model introduced in section 2.1. Next, the gradient Ri number is used:

$$Ri = \frac{\frac{g}{\Theta_0}\frac{\partial \theta}{\partial z}}{\left(\frac{\partial u}{\partial z}\right)^2 + \left(\frac{\partial v}{\partial z}\right)^2}\,, \tag{16}$$

The eddy diffusivities $K_m = K_h$ are modelled according to Eq. (5) with a parameterised turbulent mixing length. The chosen parameterisation is similar to the analytical expression suggested by Blackadar (1962) for neutral ABLs, and extended by Delage (1974) to account for stability:

$$l_m = \frac{\kappa z}{\varphi(t, Ri) + \frac{\kappa z}{\lambda_b}}\,, \tag{17}$$

where κ is the von Kármán constant and with the difference that $\varphi(t, Ri)$, which will be properly defined in equation (21), follows from the SSE and thus is a nondimensional stochastic process that replaces the use of the dimensionless shear in the original formulation (see eg. Rodrigo and Anderson (2013), Eq.18). Following Rodrigo and Anderson (2013), the value λ_b, which restrains the size of the largest turbulent eddies in neutral stratification is parametrized as:

$$\lambda_b = 2.7 \times 10^{-4}\frac{u_g}{|f_c|}\,, \tag{18}$$

where $f_c = 2\,\omega\sin(\varphi)$, with $\varphi = 40°\mathrm{N}$ and $\omega = 7.27 \times 10^{-5} s^{-1}$. The stochastic variable $\varphi(t, Ri)$ is constructed using a mixture of deterministic and stochastic formalism. Equation (15) determines the stability correction value ϕ from the surface up to some chosen height z_s (set as $z_s = 50\,\mathrm{m}$), above which a traditional scaling function $\phi_f(Ri)$ is in operation, here taken as (Cuxart et al., 2006):

$$\phi_f(Ri) = 1 + 12Ri \qquad \text{for } z > z_s\,. \tag{19}$$

Finally, the descriptions above and below z_s are joined through the logistic sigmoid function:

$$\mathrm{sig}(z) = \frac{1}{1 + \exp(-k_s(z - z_s))}\,, \tag{20}$$

where z_s is the sigmoid's midpoint, and $k_s = 0.1$ is the steepness of the curve, which regulates the sharpness of transition from ϕ to ϕ_f at the height z_s. Then the linear-convex composite is defined:

$$\varphi(t, Ri) = \phi_f(Ri)\mathrm{sig}(z) + \phi(t, Ri)(1 - \mathrm{sig}(z))\,, \tag{21}$$

and is inserted into (17). Due to the stochasticity of φ, the mixing length l_m and hence the entire turbulence closure become stochastic. The stochastic process accounts for the variation of the mixing length hypothesised to be related to intermittency of turbulence and to submesoscale mixing events (Boyko & Vercauteren, n.d.).

The stochastic process ϕ is expressed by the prognostic Eq. (15) with the data-driven scaling functions obtained in Boyko and Vercauteren (n.d.) that scale the model coefficients with the Ri number:

$$\Lambda(Ri) = 9.3 \tanh\left[0.9 \log_{10}(Ri) - 0.1\right] + 8.3\,, \tag{22}$$

$$\mathcal{V}(Ri) = 10^{(0.4 \log_{10}(Ri) + 0.2)}\,, \tag{23}$$

$$\Sigma(Ri) = 10^{(0.8 \tanh[0.6 \log_{10}(Ri) - 0.8] + \sigma_s)}\,, \tag{24}$$

where σ_s (see Eq. (24)) regulates the intensity of the stochastic component of Eq. (15). The parameter σ_s can be adjusted in the range $[-1, 0]$. The value $\sigma_s = -1$ equals to the considerably low intensity of the noise, such that the solution of Eq. (15) becomes nearly deterministic. The value $\sigma_s = 0$ corresponds to the level of the Fluxes Over Snow Surfaces Phase II (FLOSS2) dataset and models relatively intense perturbations. All details related to the data-driven identification of the scaling function are given in Boyko and Vercauteren (n.d.) and are not repeated here. An example realisation of the stochastic stability equation for different levels of σ_s can be visualised in that paper, Figure 6. Finally, the data-driven identification of the parameters was done based on hourly time units. The constant $\tau_h = 3600$ in Eq. (15) transforms the units of the equation into seconds for the numerical implementation. Consider that due to $\mathbb{E}(dW_t)^2 = dt$, the process dW_t has the units of $\sqrt{\text{time}}$ (Horsthemke, 1984), and hence the transformation of units for the noise (stochastic) term is different than in the drift (deterministic) term.

3 Numerical Implementation

3.1 Discretisation

Equations (10) – (15) are discretized and solved using the Finite Element Method (FEM) library FEniCS (Alnæs et al., 2015; Logg et al., 2012), which performs the discretization of the nonlinear system using the FEM. Dunbar et al. (2008) also applied the FEM to simulate the SBL and showed that an adaptive grid refinement approach significantly increases the accuracy of the solution. Nevertheless, the adaptive grid technique is not used here. Instead, a fine grid resolution is set and found to be affordable for the single-column proof-of-concept study done here. Equation (14) is discretized with the explicit EULER method in time. The stochastic Eq. (15) is discretized with the MILSTEIN method in time (Lord et al., 2014).

Two different numerical grids are used in the discretization. For the variables u, v, θ, and e, a power-three transform on the z-axis is imposed to improve the resolution of the gradients in the vicinity of the surface. Such a non-equidistant grid cannot be used to solve the stochastic Eq. (15) due to the sampling algorithm, which utilizes a FOURIER transform. The FOURIER transform is used because the sampling procedure of the noise process uses a correlation lengthscale, such that the random perturbations are correlated in space. The interested reader is referred to Boyko (2022) for full details on this implementation and on the definition of the correlation lengthscale. Furthermore, since the stochastic perturbations are included in the lower portion of the boundary layer ($z < 50\,\mathrm{m}$) the stochastic grid is confined to the lower portion of the computational domain.

This saves computational resources and improves the vertical resolution of the stochastic perturbations. Figure 1 shows the description of the numerical grids along with the computation steps to obtain the hybrid stochastic mixing length correction φ defined by (21).

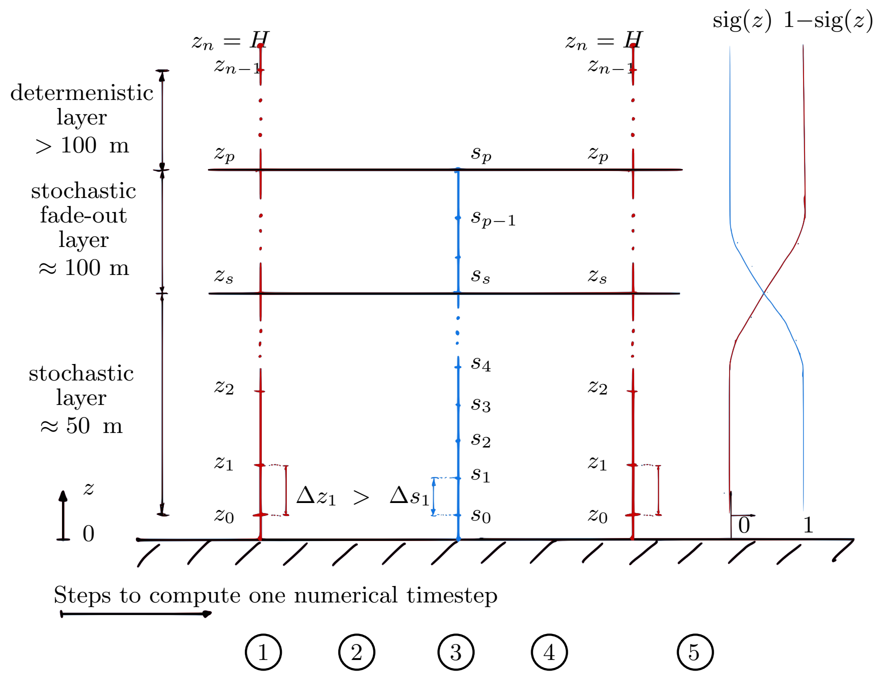

Figure 1. The computation of the hybrid stochastic mixed length correction φ using two different grids. The z-grid in red is non-equidistant and is used to solve the variables u, v, θ, e. The s-grid in blue is equidistant and is used to solve the stochastic variables ϕ. The circled numbers below mark the five steps to calculate the value of φ. 1) Calculate the Ri number on the grid z. 2) Interpolate the Ri number on the equidistant s-grid. 3) Evolve the stochastic variable ϕ to the next time step by solving the SSE. 4) Interpolate ϕ to the non-equidistant grid within the height z_p. 5) Compute the liner-convex combination between the deterministic ϕ_f and stochastic ϕ variables on the z grid using the sigmoid function sig(z) (see Eq. (20)).

The total domain is organized into three sub-layers, as indicated on the left in Fig. 1. The stochastic layer reaches up to the height $z_s = 50$ m. In this sub-domain, the dynamic of the stability correction variable is entirely determined by the Stochastic Differential Equation (SDE) (15). From the height of z_s up to the height $1.2z_s < z_p < 2.0z_s$, the stochastic fade-out layer is defined. The layer is responsible for the smooth transition from the stochastic to the deterministic value. The transition layer is also responsible for providing sufficient buffer length needed by the sampling algorithm to obtain random structures which do not re-enter the domain at the surface s_0. Indeed, without a buffer layer, the stochastic structures would re-enter at the surface due to periodicity assumptions of the Fourier transform used to sample to stochastic process. A linear-convex combination is performed between the stochastic ϕ and the deterministic ϕ_f variables (see Eq. (21); also marked in Fig. 1 with the step 5). The height $z_s = 50$ m characterizes the smooth blending between stochastic ϕ and the deterministic ϕ_f variables. Its value is set slightly larger than the measurement tower that was used to calibrate the stochastic part of the model. Hence, only the lowest 50 m of the simulations have a randomized stability correction in the application of MOST.

3.2 Initial and boundary conditions

Initial conditions are set following logarithmic profiles in neutral conditions, with:

$$u(z, t=0) = \frac{u_{*,\mathrm{init}}}{\kappa} \ln(z/z_0), \tag{25}$$
$$v(z, t=0) = 0\,, \tag{26}$$

where $u_{*,\mathrm{init}} = (0.5\, C_f\, u_g^2)^{1/2}$. Here $C_f \approx 4 \times 10^{-4}$ is a tuning parameter and is adjusted such that u_g is obtained at the model top. The initial profile for e is estimated following Parente et al. (2011):

$$e(z, t=0) = a_1 \ln(z) + a_2 \tag{27}$$

The coefficients a_1 and a_2 are estimated using the following boundary values:

$$e(z = z_0, t=0) = u_{*,\mathrm{init}}^2\,(0.087)^{-1/2}, \tag{28}$$
$$e(z = H, t=0) = 0\,, \tag{29}$$

where H is the domain height. The initial profile of the potential temperature is constant $\Theta_0 = 300\,\mathrm{K}$ up to a certain height $H_c = 200\,\mathrm{m}$ and then increases according to the dry adiabatic lapse rate $\Gamma = 0.01\,\mathrm{K\ m^{-1}}$ as used by Sorbjan (2012):

$$\theta(z, t=0) = \begin{cases} \Theta_0, & \text{for } z \le H_c\,, \\ \Theta_0 + \Gamma z, & \text{for } z \ge H_c\,. \end{cases} \tag{30}$$

Regarding the boundary conditions, for the wind components no-slip conditions (Dirichlet condition) are set at the surface, while at the top boundary, the vertical gradients are set to zero (Neumann condition). A lapse rate is imposed as upper boundary condition for the potential temperature. The values of parameters of the SURANS model used in the numerical cae studies are summarized in Tab. 1.

4 Numerical Case Studies

Idealised numerical case studies are used to test the SURANS model, validate the numerical stability of the proposed stochastic turbulence closure scheme and study the resulting differences to the classical RANS model with a 1.5 order closure. The impact of the stochastic perturbations that induce intermittency and unsteady mixing is analysed by comparison to the unperturbed model in three numerical experiments differing in stability conditions. The neutral stratification is studied first. This study is a validation case where no stability correction is needed for the mixing length, hence the ensemble mean of the SURANS model should match the RANS model. Next, the strongly SBL with intermittent mixing is analyzed. The SURANS model reproduces an intermittent TKE state. When analyzing this intermittent state, the ensemble mean is not a representative measure due to non-Gaussian statistics. A more appropriate measure is the central tendency (the most probable value), and its evolution is used to evaluate the performance of the models. Those two studies are performed for a quasi-stationary case, where the geostrophic forcing and the soil properties are constant in time. The stochastic perturbations may also alter the solution under conditions with variable forcing, and this aspect is analyzed in a third numerical study.

4.1 Neutral Boundary Layer

As a first numerical experiment, a neutral boundary layer is simulated with the SURANS model. This experiment validates that the central tendency of the SURANS model, i.e. the most probable value of an ensemble of realisations, is equivalent to the RANS solution. The initial conditions are set as neutral profiles as described in Sec. 3 and the

Table 1. Summary of the parameter values of the SURANS solver. The parameters marked with '–' are given individually in the following case studies.

Description	**Symbol**	**Value**	**Source**
Total simulation time [h]	T_end_h	–	set
Timestep [s]	dt	–	tuned
Grid resolution (z grid)	Nz	100	set
Roughness length [m]	z_0	0.044	(Acevedo et al., 2021)
Roughness length for heat [m]	z_{0h}	$z_0 \times 0.1$	(Sanz Rodrigo et al., 2017)
Domain height [m]	H	300	set
Restoring temperature [K]	θ_g	290	set
Reference potential Temperature [K]	Θ_0	300	set
Air density [kg/m^3]	ρ	1.225	set
Air specific heat capacity [J/kg/K]	c_p	1005	set
Soil heat capacity[J/m^2/K]	C_g	1.79e5	(Acevedo et al., 2021)
Net radiation	R_n	–	(Acevedo et al., 2021)
Geostrophic wind [m/s]	u_g	–	set
Geostrophic wind [m/s]	v_g	0	set
Latitude [°N]	φ	40	FLOSS2 dataset
CORIOLIS parameter [rads/s]	f_c	9.34e-05	FLOSS2 dataset
Atmospheric lapse rate [K/m]	Γ	0.01	(Rodrigo & Anderson, 2013)
Relaxation time scale [s]	τ_r	3600×5	tuned
Minimum TKE level [m^2/s^2]	min_tke	10^{-4}	tuned
Turbulent PRANDTL number for BC	Pr_t	0.85	(Želi et al., 2019)
Eddy viscosity constant [–]	α	0.46	(Rodrigo & Anderson, 2013)
Dissipation constant [–]	α_ε	0.1	tuned
Sub-mesoscale intensity [–]	σ_s	-0.07	FLOSS2 dataset
Stochastic model height [m]	z_s	50	FLOSS2 dataset
Covariance length [m]	l_z	20	FLOSS2 dataset
Von Kármán's constant [–]	κ	0.41	(Rodrigo & Anderson, 2013)

Table 2. Relevant solver settings for the numerical study of the neutral layer.

Description	**Symbol**	**Value**
Total simulation time [h]	T_end_h	15
Time step [s]	dt	10
Grid resolution (z grid)	Nz	100
Domain height [m]	H	300
Restoring temperature [K]	θ_s	300
Reference potential Temperature [K]	Θ_0	300
Net radiation [W m^{-2}]	R_n	0
Geostrophic wind [m/s]	u_g	5

simulation period is set to 15 hours. The solver specific settings for this experiment are given in Tab. 2 and the rest in Tab. 1. The forcing parameters are set to be constant. The stratification is controlled with two parameters of the surface energy balance implemented in Eq. (14), namely the net radiation R_n, and the restoring temperature θ_s, which together control the degree of surface cooling. To simulate neutral conditions the net radiation is set to 0, hence forbidding radiative cooling. The restoring temperature θ_s is set equal to the initial air temperature, ensuring strictly neutral stratification.

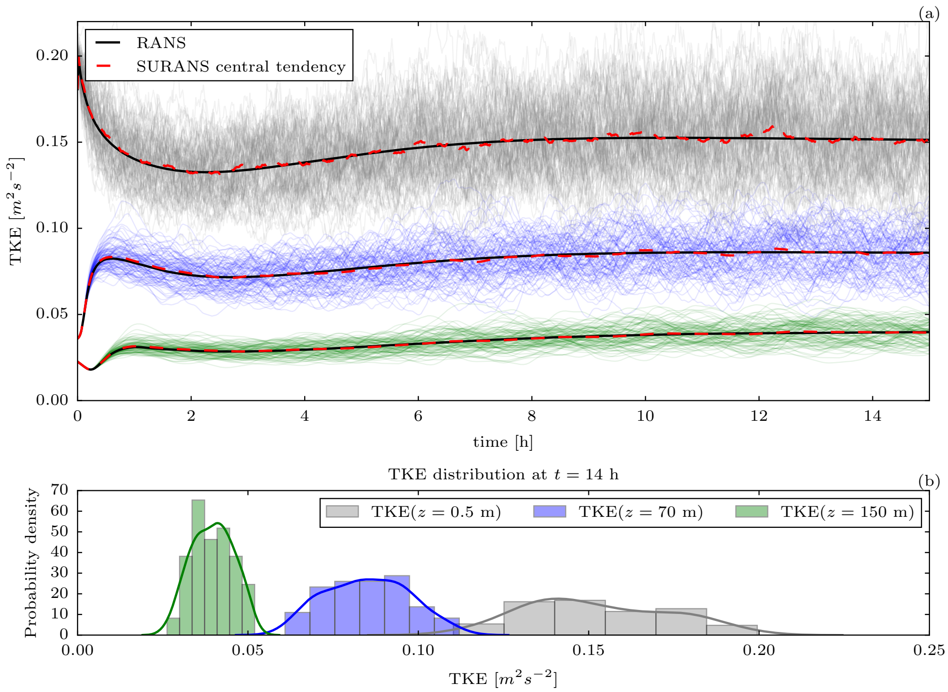

Figure 2. Comparison of the predicted TKE by the SURANS and RANS models in the condition of neutral stratification ($Ri = 0$) for three heights ($z = 0.5, 70, 150\,\mathrm{m}$). The evolution of TKE is shown in (a) and the corresponding color legend is given in (b). Panel (a) shows the RANS solution with a solid black line. The many lines in different colors indicate the 100 realizations of the SURANS model for their heights. The central tendency of the SURANS model is indicated by a dashed red line. The respective probability distribution of the TKE ensemble at $t = 14\,\mathrm{h}$ is given in panel (b).

Figure 2 shows the comparison of the TKE at three different heights ($z = 0.5, 70, 150\,\mathrm{m}$) for simulations with and without the stochastic mixing induced by the stochastic stability equation. A quasi steady-state solution is reached approximately after six hours with the RANS model. The central tendency of the SURANS model, which is estimated from averaging over 100 realizations, is nearly identical to the solution of the RANS model. The regularity of the sample paths (indicated with the thin colored lines) varies across the height. More rapid fluctuations are found closer to the surface (sample paths in gray), and smooth oscillations with smaller variances occur at $z = 150\,\mathrm{m}$ (sample paths in green). The stochastic mixing length equation is only active up to the height $z = 100\,\mathrm{m}$. As indicated by the sample paths in green ($z = 150\,\mathrm{m}$), the variability induced at the surface is propagating into the upper levels of the boundary layer. Hence the stochastic MOST impacts the upper boundary layer.

The distributions of the TKE from the 100 SURANS simulations are close to being Gaussian, but more importantly, those are symmetrical. This symmetry indicates that the modeled type of turbulence is such that the perturbed solutions maintain their path around the central tendency, which itself is very close to the deterministic RANS solution. Hence in this neutral case, the stochastically added effect of unresolved random mixing events is small enough that the TKE remains in statistical equilibrium in the perturbed model. As shown in the next stably stratified experiments, the equilibrium becomes weaker and more sensitive to the perturbations at a larger Ri number, leading to turbulence intermittency.

4.2 Stably Stratified Boundary Layer

The next experiment considers a stably stratified boundary layer in the presence of random mixing events. Similar to the neutral case, the initial conditions are given in Sec. 3, and the simulation period is set to 15 hours. The solver-specific settings for this experiment are given in Tab. 3 and the rest in Tab. 1. The forcing parameters are set to be constant. The stratification is imposed with two mechanisms, the first being the

Table 3. Relevant solver settings for the numerical study of the stably stratified boundary layer.

Description	Symbol	Value
Total simulation time [h]	T_end_h	15
Time step [s]	dt	5
Grid resolution (z grid)	Nz	100
Domain height [m]	H	300
Restoring temperature [K]	θ_s	290
Reference potential Temperature [K]	Θ_0	300
Net radiation [W m^{-2}]	R_n	-30
Geostrophic wind [m/s]	u_g	5

difference between the restoring (soil) temperature of 290 K and the potential temperature of the air 300 K, and the second being a radiative cooling enhancing the stratification. The net radiation of -30 W m^{-2} is selected following Acevedo et al. (2021) and considered as the FLOSS2 dataset average value. This setup may describe a typical cloud-free night in springtime.

Figure 3 illustrates the solution of the SURANS model. The TKE at the height $z = 20$ m is compared against the solution of the RANS model using several statistical metrics. In Fig. 3a, a characteristic signature of intermittent TKE simulated with the SURANS model is highlighted in blue. Thin gray lines display other realizations of the stochastic model. Note the two different types of spikes found at $t = 6$ h and $t = 10$ h. Their magnitude is significantly larger than the ensemble mean (solid yellow) and the central tendency (solid red). The duration of these events is approximately one hour and falls within the characteristic range of sub-mesoscale motions (Mahrt, 2014; Vercauteren et al., 2016).

The ensemble mean TKE of the simulations, shown in Fig. 3, is slightly above the RANS prediction. However, the central tendency is significantly smaller and indicates that it is likely to observe an absence of turbulent mixing. The heavy tail in the ensemble distributions is significant and related to sporadic rare events. Some realizations of the model (not shown) predict a low TKE level throughout the entire simulation period. The wide variety of TKE signatures highlights the representative capabilities of the stochastic model. The central tendency is estimated based on the TKE distribution obtained through 100 model runs at $t = 14$ h and shown in Fig. 3b. The solid black line represents the prediction of the RANS model for comparison. The solid yellow line is the ensemble mean of the SURANS model, and the solid red line is the central tendency. The central tendency is estimated from the Probability Density Function (PDF), which is fitted to the histogram by applying the KDE method (Scott, 2015). The estimation is poor and violates the boundary condition on the left side. Nevertheless, the KDE is a time-efficient method to approximate the most probable value. The histogram indicates a smaller

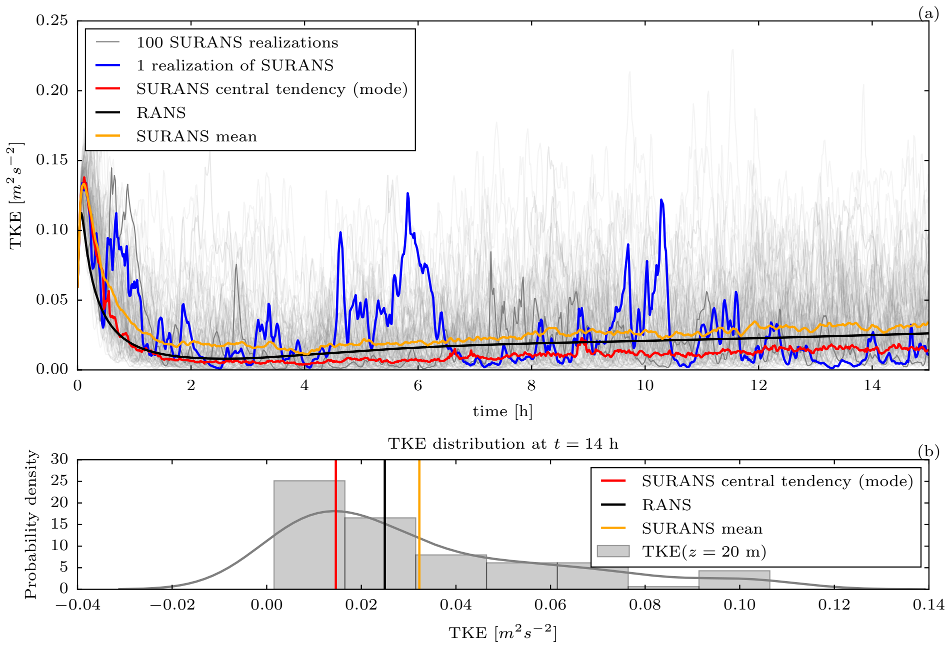

Figure 3. Comparison of SURANS and RANS models predicted TKE under the condition of strongly stable stratification (mass $Ri \approx 0.6$) for height $z = 20$ m. For the visualization of the Ri number profiles, see Fig. 7. The evolution of the TKE is shown in (a). The ensemble distribution of 100 sample paths of the SURANS model at $t = 14$ h is shown in panel (b) along with the fitted probability density function (solid gray line) using a KDE method. The thin gray lines show the 100 realizations of the SURANS model.

value of the central tendency than the estimated one. A better estimation can be achieved if a specific distribution type is assumed. However, one should keep in mind that the distribution type is influenced by the stratification. This dependence makes the fitting task less trivial and we refrain from using more complex estimation approaches for studying the distributions of the TKE.

Figure 4 shows a selected realisation of the ensemble of simulations including clearly intermittent features. The largest intensity of each burst of TKE is found at the surface. The stochastic correction of the turbulent diffusion can in principle lead to intermittent patches detached from the ground (see Fig.6 in Boyko and Vercauteren (n.d.) for such an example), as is found to occur in observations (see eg. Sun et al. (2002)). Still, in the simulation we cannot find any turbulent patches that are clearly detached from the surface. The bursts are absent aloft because the turbulent diffusion is multiplied with the gradient of the mean wind, and hence the spatial distribution of the TKE is intrinsically constraint by the wind gradient. A slight inclination (as somebody brushed it from left to right) in the bursts is also present. Some events show that turbulence is still maintained away from the surface (see Fig. 4a $t = 3.5$ h and $t = 5$ h), leading to TKE that is decoupled from the surface. Here the flow is forced with a steady mean wind. Changing the forcing changes the gradient away from the surface and could provide room for the stochastic perturbations to appear at higher levels due to localised shear accelerations.

The impact of the randomised model on the temperature evolution is visualized in Fig. 5. It is evident that in the case of stochastic perturbations, the mixing is performed

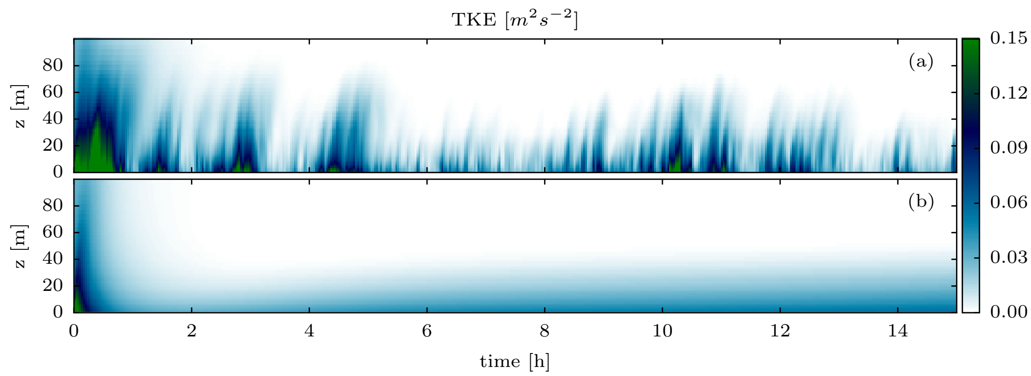

Figure 4. Temporal evolution of the profiles of TKE for a realization of the SURANS (a) and RANS (b) models. The color bar applies to both panels.

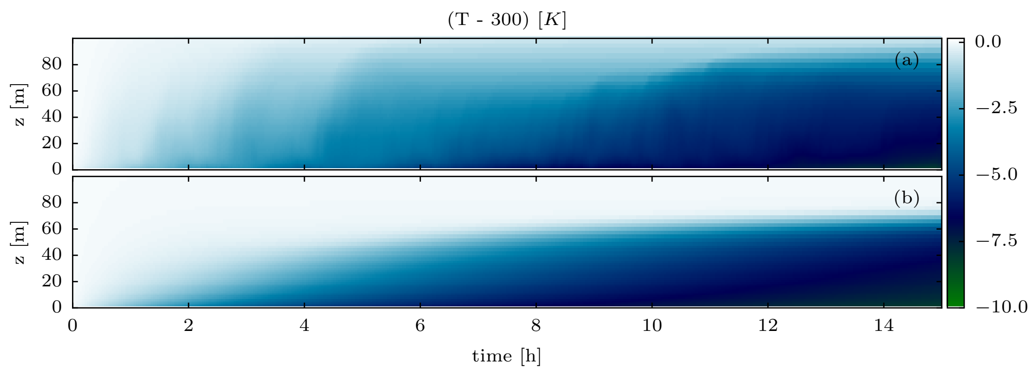

Figure 5. Temporal evolution of the temperature profiles for one realization of the SURANS (a) and RANS (b) models. The color bar is valid for both panels.

faster. The mixing rate is higher, and the temperature inversion is also shifted up and is less abrupt. The temperature profile changes its shape in an unsteady way (compare Fig. 5a to 5b), related to the activity of the intermittent burst periods (see Fig. 4a). The stochastic model shows a qualitatively different solution of the temperature inversion. The profiles of the dominant wind velocity component u are visualized in Fig. 6. A repeating pattern of the TKE bursts is visible in Fig. 6a, comparable to the pattern seen in Fig. 4a. The dominant stochastic turbulent diffusion dictates the boundary layer shape as a consequence of random mixing events. Figure 7 shows the evolution of the profiles for the Ri number. The SURANS model predicts a strongly unsteady local Ri number, but the bulk Ri number is computed for the layer between the z_0 level and $z = 80$ m. Deviations are found during random mixing events when the temperature profile is mixed sporadically, reducing the local bulk Ri number (compare with Fig. 5).

4.3 Variable Geostrophic Wind and Net Radiation

In the last case study, a time varying forcing scenario is considered, thereby studying the impact of the stochastic perturbations during transient states. The initial conditions are given in Sec. 3, and the simulation period is set to 30 hours, which is longer than the average nighttime. In this experiment, the focus lies on computing the transitions between weakly and strongly SBL, as in Maroneze et al. (2019); Acevedo et al.

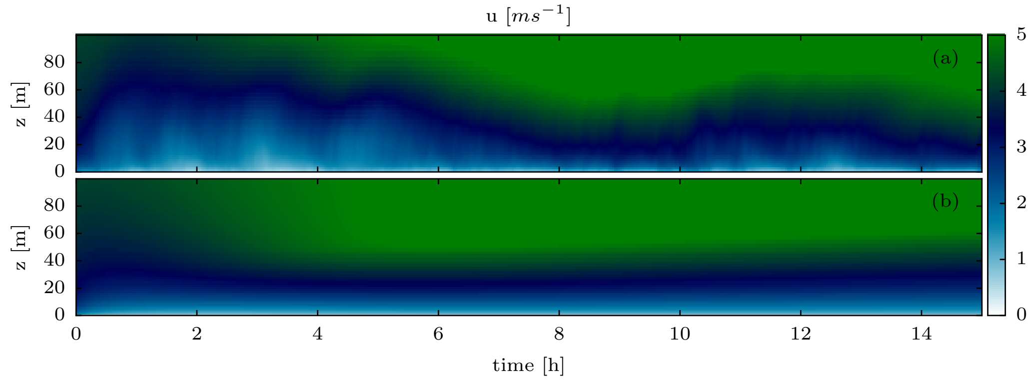

Figure 6. Temporal evolution of the wind profiles (u component) for one realization of the SURANS and RANS models. The color bar is valid for both panels.

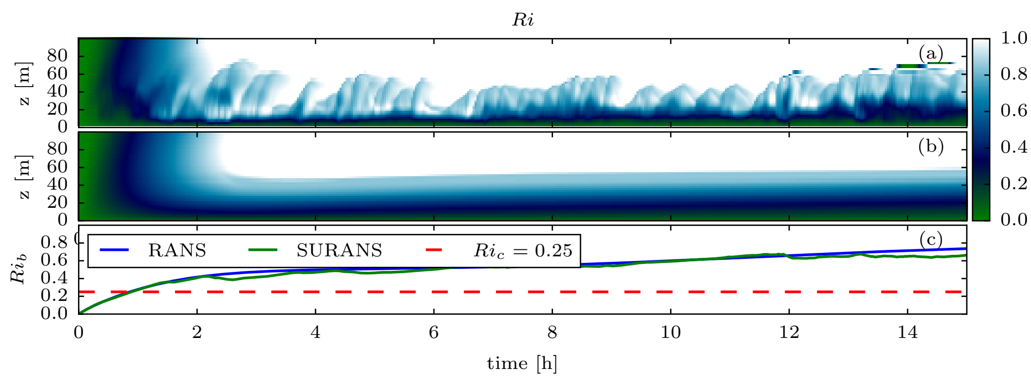

Figure 7. Temporal evolution of the Ri number profile for a realization of the SURANS (a) and RANS (b). The color bar applies to panels (a) and (b). Panel (c) shows the bulk Ri number calculated from the surface to $z = 80$ m.

(2021). The novelty of this study is that random mixing events are included in the model, representing unresolved features of the flow. The nonstationary forcing is chosen such that the geostrophic wind increases gradually at some given time, while the radiative cooling increases once from 0, to go back to a 0 value later in the simulation. The simulation thereby covers four possible forcing combinations, alternating in time as shown in Fig. 8a. The solver-specific settings for this experiment are given in Tab. 4 and the rest in Tab. 1.

The temporal evolution of the TKE at the height of $z = 9\,\mathrm{m}$ is shown in Fig. 8b), with additional exerts showing the profiles for the variables e, θ and $U = \sqrt{u^2 + v^2}$ at three different times (note the arrows in Fig. 8b). The quantities visualised in Fig. 8 are:

- The 100 realizations of the SURANS model (gray, thin lines).
- The central tendency (solid red), estimated as the most probable value from the fitted distribution (see Fig. 3).
- The noise-free limit of the SURANS model. In this case, the stochastic equation is solved once with a sufficiently low value of the noise, such that the dynamical evolution can be considered deterministic (solid yellow line). The noise-free limit

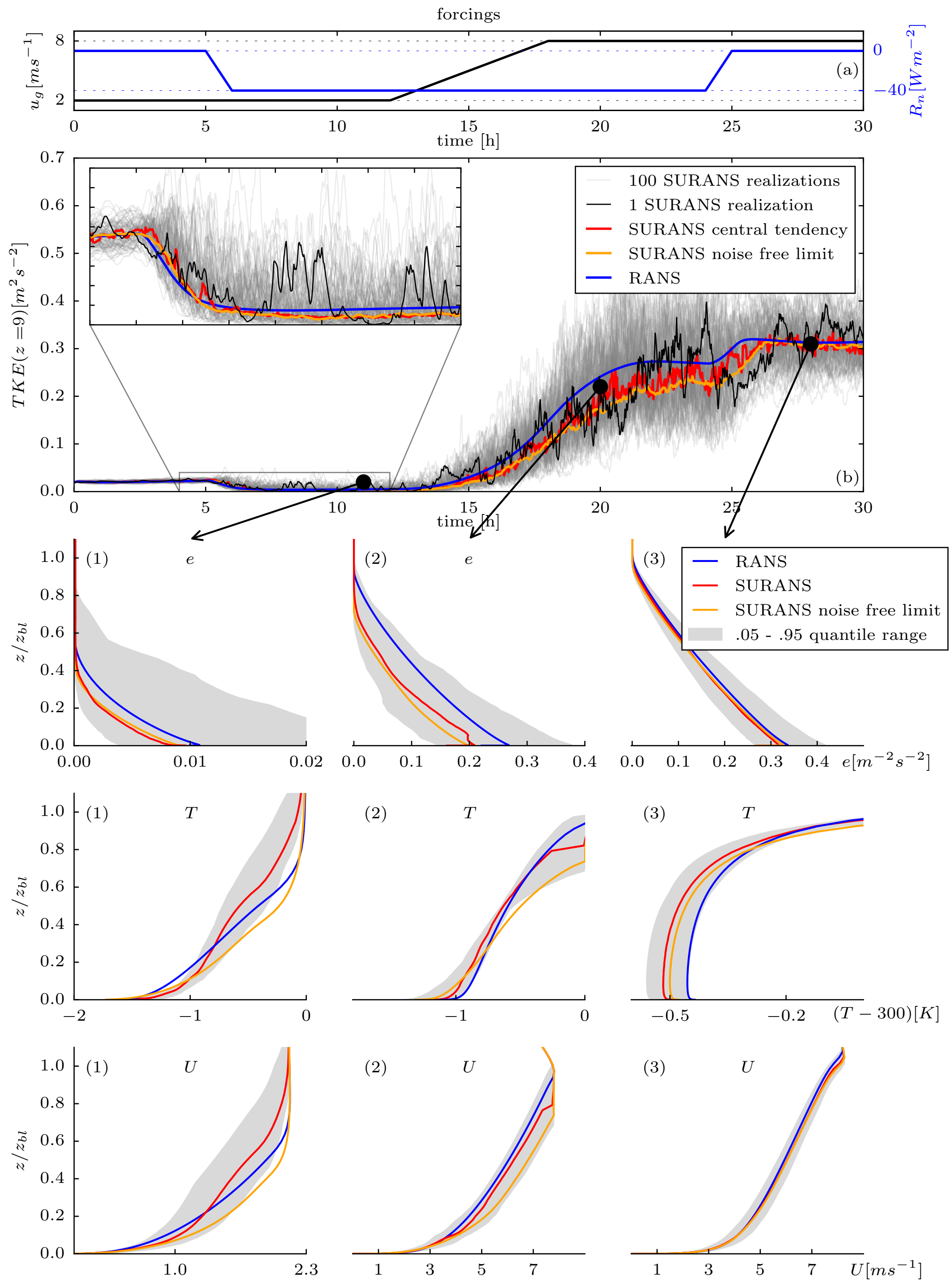

Figure 8. Solution of the SURANS model with variable forcing parameters R_n (net radiation) and the geostrophic wind u_g. The total simulation period is 30 hours. The nudging time scale is set to 5 hours. Panel (b) shows the evolution of TKE at 9 m for 100 realizations, marked with gray lines. The zoom area highlights the transition to stable stratification in weak winds by increasing net radiation. The evolution of the forcing is shown in a). The sub-images in b) show profiles of the variables at 3 different times marked with black dots in b). The SURANS profiles represent the central tendency, with the gray area showing the quantile range. The boundary layer height z_{bl} used for normalization is 50 m (first period), 200 m (second period), 240 m (third period).

Table 4. Relevant solver settings for the numerical study with unsteady forcing variables.

Description	**Symbol**	**Value**
Total simulation time [h]	T_end_h	30
Time step [s]	dt	2
Grid resolution (z grid)	Nz	100
Domain height [m]	H	300
Restoring temperature [K]	θ_s	300
Reference potential Temperature [K]	Θ_0	300
Net radiation [W m^{-2}]	R_n	variable (see Fig. 8a)
Geostrophic wind [m/s]	u_g	variable (see Fig. 8a)

is introduced to eliminate the effect of the difference between the MOST stability function and the deterministic steady-state of the prognostic Eq. (15) (the expected value of the random variable). One realization of the SURANS model is emphasized to highlight the rare events during the stable low-wind conditions (solid black line).

- The prediction of the RANS model (solid blue line).

To study the impact of the applied perturbations, we first compare a solution of SURANS in the noise-free limit with the central tendency estimated from the 100 realizations of the stochastic model (see yellow and red lines in Fig. 8). There are no significant differences in the TKE (see 8b and the corresponding profiles). However, there is a substantial impact of the applied perturbations on temperature and velocity profiles. With stochasticity, the temperature is mixed more effectively during the stably stratified period and the mixing extends above the average boundary layer height (see Fig. 8 panel (1)). The central tendency of the velocity profile experiences a deceleration compared to the noise-free limit. For higher geostrophic winds in the second visualised period, the perturbation of the turbulent diffusion is propagated to the top of the boundary layer (200 m), although the actual perturbations are limited at 50 m.

As a next step, we compare the reults of the SURANS and the RANS models. The RANS solution (blue line) predicts higher levels of TKE than the central tendency (red line) obtained by the SURANS model, throughout the entire simulation. Despite this lower level of TKE simulated by the SURANS model, transport of temperature and velocity is enhanced (see Fig. 8 panels (1)). This nontrivial effect may result from non-equilibrium statistics in the stochastic formulation of the turbulent mixing length. The variability of results is visualised through the gray area in Figure 8, representing the $0.05 - 0.95$ quantile range of the 100 different model runs. For stable stratification (see Fig. 8 panels (1)), the quantile range for the TKE is asymmetrical, showing the largest spread closest to the surface. In neutral conditions, the quantile range is symmetrical (see Fig. 8 panels (3)). The model ensemble spread for the TKE profile is significantly different than the ensemble spread for the temperature and velocity profiles. The largest ensemble spread for temperature and velocity profiles is found in the middle of the boundary layer, with lower spread at the surface and the boundary layer top.

Observing the individual simulation paths (see Fig. 8b thin gray lines), the impact of the random perturbations on the transition periods can be analysed. The inset in Fig. 8b highlights a transition from neutral to stable stratification induced by the onset of radiative cooling. The central tendency and the noise-free limit of the SURANS model overlap during the transition. However, multiple individual realizations (thin gray lines) show a pronounced tendency to delay the transition rather than induce early transition. In contrast, by transitioning from low wind to high wind (see Fig. 8b from $t = 15$ to

$t = 20$), the solution paths can show both early and delayed transitions. The individual simulation paths also show that during this period where u_g increases, the variance in the TKE increases as well. When radiative cooling is interrupted (see $t = 25\,\mathrm{h}$), the variance reduces to some lower value. The reason for this is the parametrization of the noise term in the stochastic equation, which only scales with the Ri number. This scaling was identified by Boyko and Vercauteren (n.d.), but possibly other dependencies could be investigated.

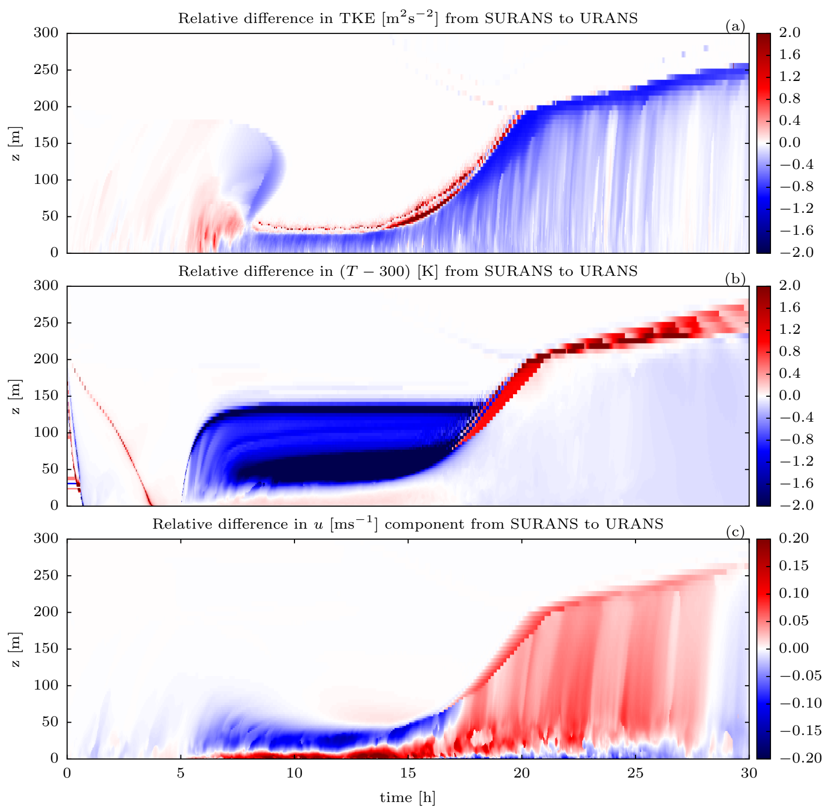

Figure 9. The relative difference in profiles between the SURANS (the central tendency of 100 realizations) and the RANS model according to the numerical study in Fig. 8. The red color denotes the area where the variables of the SURANS model have larger magnitude than those of the RANS model. The white color denotes no differences. Panel (a) shows the TKE, (b) the temperature ($-2\ [K] < (T-300)[K] < 0\ [K]$), and (c) the dominant u component of the wind. The forcing variables change with time and are shown in Fig. 8a. Condition of stable stratification for $t \in (5, 15)\,\mathrm{h}$ and condition of high wind pressure for $t \in (5, 15)\,\mathrm{h}$.

The relative differences in space and time of solutions obtained through the SURANS and RANS models are shown in Figure 9, where panel a shows the differences in TKE. The transition from blue to white color (no difference) indicates approximately the boundary layer height. The boundary layer grows after $t = 15$ as the geostrophic wind is increased. For the time $t > 25\,\mathrm{h}$ the radiative cooling is interrupted, and the central tendency of the SURANS model becomes very similar to the RANS solution. For the time $t > 6\,\mathrm{h}$ the value of the TKE predicted by the SURANS model is 50% smaller than predicted by RANS on average, indicating a shallower boundary layer (as seen in the TKE profiles of Fig. 8). Figure 9b shows the relative difference in the temperature. Within the boundary layer (where relative differences in TKE are found) the differences between

SURANS and RANS are insignificant. At the boundary layer top, the SURANS model deviates from the RANS solution. For the stably stratified conditions ($t \in (5, 15)$), the central tendency of the SURANS solution predicts almost a 200% lower value of the temperature than the RANS model for a large area above the boundary layer (see the blue area in Fig. 9b). At the same time, the differences at the surface are relatively small. This can be explained by the enhanced transport due to intermittent turbulence. By construction, the stochastic perturbations start to fade away above $z > 50\,\mathrm{m}$. At the same time, the boundary layer height is approximately 25 m, such that the stochastic perturbations determine the mixing of temperature. The red area at the top of the boundary layer in Fig. 9b for $t > 17\,\mathrm{h}$ (the high-wind regime) means that the central tendency of the SURANS model is predicting an increased value of the temperature relative to the RANS model. Hence, the errors produced in the stable regime ($5 < t < 15\,\mathrm{h}$) are propagated into the high-wind regime ($t > 20\,\mathrm{h}$) at the boundary layer top. This findings suggest that the altered transport of temperature and possibly moisture (although not included in this model) may impact the creation of clouds in the early morning with increasing geostrophic winds.

5 Summary and conclusions

A stochastic stability equation, suggested by Boyko and Vercauteren (n.d.) to introduce a stochastic parameterisation of unsteady turbulence, was implemented and tested in this study. The previous data-driven analyses showed that the stochastic model for turbulent mixing could in principle accommodate both the short-term intermittent behaviour of turbulence and the long-term averaged mixing, as validated against field measurements. The stochastic model parameters in the SURANS model were found to scale with the local gradient Ri number (Boyko & Vercauteren, n.d.). As a result, the intermittent statistical properties of the modelled TKE are changing continuously as a function of flow stability. In this paper, the stochastic parameterisation was implemented in a SURANS single-column model extended from a RANS model with 1.5 closure. The stochastic stability equation can in principle also be used in a first-order closure model. The impact of the randomized model was evaluated through selected idealised numerical case studies with varying stability conditions. In the current implementation, the stochastic equation is confined to the lower portion of the boundary layer and is blended with a deterministic model above. It is unknown at this stage if the proposed closure is locally valid in the outer boundary layer.

The proposed framework was found to be numerically stable. In the strongly stable condition it is advisable to use an adaptive time stepping in the time integration to avoid abrupt numerical instabilities. These instabilities come from the strong stratification in combination with the stochastic events. Due to the randomness of the stochastic events it can happen that negative TKE is induced. Any mechanism preventing the solver to run negative TKE values is necessary for strongly stable conditions.

In neutral conditions, the stochastic parameterisation was found not to have a significant impact on the statistical properties of the modelled flow, simply introducing limited variability compared to the RANS reference model. Within the regime of strong stratification, the SURANS model adequately represents intermittent TKE patterns. The intermittent mixing events affect the boundary layer height. In conditions of weak stratification and large geostrophic wind speeds, the SURANS model appears to show unrealistically large variance, indicating that further model tuning may be necessary. For practical application it is advisable to limit the noise intensity in the stochastic stability equation by some critical geostrophic wind, for example. In stably stratified conditions, the SURANS model shows enhanced mixing properties in comparison to a RANS with a linear stability correction function. The temperature profile is mixed faster and reaches over larger heights. In comparison to the RANS solution, the stochastic model predicts lower temperature value just above the shallow, stably stratified boundary layer.

The effect of stochastic diffusion reaches beyond the limiting height of the perturbations. This results in qualitatively different profiles compared to the RANS solutions in the outer boundary layer. Furthermore, the boundary layer height becomes highly variable in strongly SBL and is determined by the random turbulent mixing events.

The presented SURANS model shows the potential to be used as an exploratory or even predictive tool. To investigate the use of the SSE for less idealized setups, future studies should validate the performance of the SURANS in controlled case studies using observational data.

6 Open Research

The computational software used in this study is publicly available at GitHub: `https://github.com/BoundaryLayerVercauteren/surans`

Acknowledgments

We are grateful to Felix Oertel for his contribution to the development of the numerical model, and to Ivan Bašták Ďurán with whom we had helpful discussions regarding the numerical stability of the code. The research was funded by the Deutsche Forschungsgemeinschaft (DFG) through grant number VE 933/2-2.

References

Acevedo, O. C., Costa, F. D., Maroneze, R., Carvalho, A. D., Puhales, F. S., & Oliveira, P. E. S. (2021, April). External controls on the transition between stable boundary-layer turbulence regimes. *Quarterly Journal of the Royal Meteorological Society*, qj.4027. Retrieved 2021-04-14, from `https://onlinelibrary.wiley.com/doi/10.1002/qj.4027` doi: 10.1002/qj.4027

Acevedo, O. C., Mahrt, L., Puhales, F. S., Costa, F. D., Medeiros, L. E., & Degrazia, G. A. (2016). Contrasting structures between the decoupled and coupled states of the stable boundary layer. *Quarterly Journal of the Royal Meteorological Society*, *142*(695), 693–702. Retrieved 2020-07-26, from `https://rmets.onlinelibrary.wiley.com/doi/abs/10.1002/qj.2693` doi: 10.1002/qj.2693

Alnæs, M., Blechta, J., Hake, J., Johansson, A., Kehlet, B., Logg, A., ... Wells, G. N. (2015). The FEniCS Project Version 1.5. *Archive of Numerical Software*, *Vol 3*. Retrieved from `http://journals.ub.uni-heidelberg.de/index.php/ans/article/view/20553` (Publisher: University Library Heidelberg) doi: 10.11588/ANS.2015.100.20553

Anfossi, D., Oettl, D., Degrazia, G., & Goulart, A. (2005). An Analysis of Sonic Anemometer Observations In Low Wind Speed Conditions. *Boundary-Layer Meteorology*, *114*(1), 179–203. Retrieved from `http://link.springer.com/article/10.1007/s10546-004-1984-4` (Publisher: Kluwer Academic Publishers) doi: 10.1007/s10546-004-1984-4

Audouin, O., Roehrig, R., Couvreux, F., & Williamson, D. (2021). Modeling the GABLS4 Strongly-Stable Boundary Layer With a GCM Turbulence Parameterization: Parametric Sensitivity or Intrinsic Limits? *Journal of Advances in Modeling Earth Systems*, *13*(3), e2020MS002269. Retrieved 2021-10-21, from `https://onlinelibrary.wiley.com/doi/abs/10.1029/2020MS002269` (_eprint: https://onlinelibrary.wiley.com/doi/pdf/10.1029/2020MS002269) doi: 10.1029/2020MS002269

Baas, P., van de Wiel, B., Van der Linden, S., & Bosveld, F. (2018). From near-neutral to strongly stratified: Adequately modelling the clear-sky nocturnal boundary layer at Cabauw. *Boundary-Layer Meteorology*, *166*(2), 217–238. (Publisher: Springer)

Baas, P., van de Wiel, B. J., Van Meijgaard, E., Vignon, E., Genthon, C., van der Linden, S. J., & de Roode, S. R. (2019). Transitions in the wintertime near-surface temperature inversion at Dome C, Antarctica. *Quarterly Journal of the Royal Meteorological Society*, *145*(720), 930–946. (Publisher: Wiley Online Library)

Berner, J., Achatz, U., Batté, L., Bengtsson, L., Cámara, A. d. l., Christensen, H. M., ... Yano, J.-I. (2017, March). Stochastic Parameterization: Toward a New View of Weather and Climate Models. *Bulletin of the American Meteorological Society*, *98*(3), 565–588. Retrieved 2022-12-12, from `https://journals.ametsoc.org/view/journals/bams/98/3/bams-d-15-00268.1.xml` (Publisher: American Meteorological Society Section: Bulletin of the American Meteorological Society) doi: 10.1175/BAMS-D-15-00268.1

Blackadar, A. K. (1962, July). The vertical distribution of wind and turbulent exchange in a neutral atmosphere. *Journal of Geophysical Research*, *67*(8), 3095–3102. Retrieved 2021-05-09, from `http://doi.wiley.com/10.1029/JZ067i008p03095` doi: 10.1029/JZ067i008p03095

Boyko, V. (2022). *Data-driven modeling of intermittent turbulence in the stably stratified atmospheric boundary layer* (Unpublished doctoral dissertation). Freie Universität Berlin. (unpublished thesis)

Boyko, V., & Vercauteren, N. (n.d.). A stochastic stability equation for unsteady turbulence in the stable boundary layer. *Quarterly Journal of the Royal Meteorological Society*, *n/a*(n/a). Retrieved from `https://rmets.onlinelibrary.wiley.com/doi/abs/10.1002/qj.4498` doi: https://doi.org/10.1002/qj.4498

Boyko, V., & Vercauteren, N. (2020, November). Multiscale Shear Forcing of Turbulence in the Nocturnal Boundary Layer: A Statistical Analysis. *Boundary-Layer Meteorology*. Retrieved 2021-01-12, from `http://link.springer.com/10.1007/s10546-020-00583-0` doi: 10.1007/s10546-020-00583-0

Cava, D., Mortarini, L., Anfossi, D., & Giostra, U. (2019, May). Interaction of Submeso Motions in the Antarctic Stable Boundary Layer. *Boundary-Layer Meteorology*, *171*(2), 151–173. Retrieved 2021-08-10, from `http://link.springer.com/10.1007/s10546-019-00426-7` doi: 10.1007/s10546-019-00426-7

Cuxart, J., Holtslag, A. A. M., Beare, R. J., Bazile, E., Beljaars, A., Cheng, A., ... Xu, K.-M. (2006, February). Single-Column Model Intercomparison for a Stably Stratified Atmospheric Boundary Layer. *Boundary-Layer Meteorology*, *118*(2), 273–303. Retrieved 2020-10-14, from `http://link.springer.com/10.1007/s10546-005-3780-1` doi: 10.1007/s10546-005-3780-1

Davy, R., & Esau, I. (2014, November). Global climate models' bias in surface temperature trends and variability. *Environmental Research Letters*, *9*(11), 114024–9. Retrieved from `http://stacks.iop.org/1748-9326/9/i=11/a=114024?key=crossref.62a944a006fca4eb162e69a83af29733` (Publisher: IOP Publishing) doi: 10.1088/1748-9326/9/11/114024

Delage, Y. (1974). A numerical study of the nocturnal atmospheric boundary layer. *Quarterly Journal of the Royal Meteorological Society*, *100*(425), 351–364. Retrieved 2023-03-02, from `https://onlinelibrary.wiley.com/doi/abs/10.1002/qj.49710042507` (_eprint: https://onlinelibrary.wiley.com/doi/pdf/10.1002/qj.49710042507) doi: 10.1002/qj.49710042507

Derbyshire, S. (1999). Stable Boundary-Layer Modelling: Established Approaches and Beyond. *Boundary-Layer Meteorology*, *90*(3), 423–446. Retrieved from `http://link.springer.com/10.1023/A:1001749007836` (Publisher: Kluwer Academic Publishers) doi: 10.1023/A:1001749007836

Dunbar, T. M., Hanert, E., & Hogan, R. J. (2008, September). A One-Dimensional

Finite-Element Boundary-Layer Model with a Vertical Adaptive Grid. *Boundary-Layer Meteorology*, *128*(3), 459–472. Retrieved 2021-05-24, from http://link.springer.com/10.1007/s10546-008-9297-7 doi: 10.1007/s10546-008-9297-7

Edwards, J. M., Beljaars, A. C. M., Holtslag, A. A. M., & Lock, A. P. (2020, December). Representation of Boundary-Layer Processes in Numerical Weather Prediction and Climate Models. *Boundary-Layer Meteorology*, *177*(2), 511–539. Retrieved 2021-08-24, from https://doi.org/10.1007/s10546-020-00530-z doi: 10.1007/s10546-020-00530-z

Esau, I., Tolstykh, M., Fadeev, R., Shashkin, V., Makhnorylova, S., Miles, V., & Melnikov, V. (2018, December). Systematic errors in northern Eurasian short-term weather forecasts induced by atmospheric boundary layer thickness. *Environmental Research Letters*, *13*(12), 125009. Retrieved 2022-12-13, from https://dx.doi.org/10.1088/1748-9326/aaecfb (Publisher: IOP Publishing) doi: 10.1088/1748-9326/aaecfb

Garratt, J. R. (1994). The atmospheric boundary layer. *Earth-Science Reviews*, *37*(1-2), 89–134. (Publisher: Elsevier)

Grachev, A. A., Fairall, C. W., Persson, P. O. G., Andreas, E. L., & Guest, P. S. (2005, August). Stable Boundary-Layer Scaling Regimes: The Sheba Data. *Boundary-Layer Meteorology*, *116*(2), 201–235. Retrieved 2023-05-11, from https://doi.org/10.1007/s10546-004-2729-0 doi: 10.1007/s10546-004-2729-0

Holtslag, A. A. M., Svensson, G., Baas, P., Basu, S., Beare, B., Beljaars, A. C. M., ... Van De Wiel, B. J. H. (2013, November). Stable Atmospheric Boundary Layers and Diurnal Cycles: Challenges for Weather and Climate Models. *Bulletin of the American Meteorological Society*, *94*(11), 1691–1706. Retrieved 2020-07-26, from https://journals.ametsoc.org/bams/article/94/11/1691/60301/Stable-Atmospheric-Boundary-Layers-and-Diurnal doi: 10.1175/BAMS-D-11-00187.1

Horsthemke, W. (1984). Noise Induced Transitions. *Non-Equilibrium Dynamics in Chemical Systems*, 150–160. Retrieved 2021-02-09, from https://link.springer.com/chapter/10.1007/978-3-642-70196-2_23 (Publisher: Springer, Berlin, Heidelberg) doi: 10.1007/978-3-642-70196-2_23

Kähnert, M., Sodemann, H., Remes, T. M., Fortelius, C., Bazile, E., & Esau, I. (2022, November). Spatial Variability of Nocturnal Stability Regimes in an Operational Weather Prediction Model. *Boundary-Layer Meteorology*. Retrieved 2022-11-21, from https://doi.org/10.1007/s10546-022-00762-1 doi: 10.1007/s10546-022-00762-1

Køltzow, M., Casati, B., Bazile, E., Haiden, T., & Valkonen, T. (2019, August). An NWP Model Intercomparison of Surface Weather Parameters in the European Arctic during the Year of Polar Prediction Special Observing Period Northern Hemisphere 1. *Weather and Forecasting*, *34*(4), 959–983. Retrieved 2023-02-07, from https://journals.ametsoc.org/view/journals/wefo/34/4/waf-d-19-0003_1.xml (Publisher: American Meteorological Society Section: Weather and Forecasting) doi: 10.1175/WAF-D-19-0003.1

Lan, C., Liu, H., Katul, G. G., Li, D., & Finn, D. (2022). Turbulence Structures in the Very Stable Boundary Layer Under the Influence of Wind Profile Distortion. *Journal of Geophysical Research: Atmospheres*, *127*(20), e2022JD036565. Retrieved 2022-11-10, from https://onlinelibrary.wiley.com/doi/abs/10.1029/2022JD036565 (_eprint: https://onlinelibrary.wiley.com/doi/pdf/10.1029/2022JD036565) doi: 10.1029/2022JD036565

LeMone, M. A., Angevine, W. M., Bretherton, C. S., Chen, F., Dudhia, J., Fedorovich, E., ... Weil, J. C. (2018, January). 100 Years of Progress in Boundary Layer Meteorology. *Meteorological Monographs*, *59*, 9.1–9.85. Retrieved from http://journals.ametsoc.org/doi/10.1175/AMSMONOGRAPHS-D-18-0013.1 doi: 10.1175/AMSMONOGRAPHS-D-18-0013.1

Logg, A., Mardal, K.-A., & Wells, G. (Eds.). (2012). *Automated Solution of Differential Equations by the Finite Element Method.* Springer Berlin Heidelberg. Retrieved from https://doi.org/10.1007/978-3-642-23099-8 doi: 10.1007/978-3-642-23099-8

Lord, G. J., Powell, C. E., & Shardlow, T. (2014). *An introduction to computational stochastic PDEs* (No. 50). New York, NY, USA: Cambridge University Press.

Louis, J.-F. (1979, September). A parametric model of vertical eddy fluxes in the atmosphere. *Boundary-Layer Meteorology*, *17*(2), 187–202. Retrieved from https://link.springer.com/article/10.1007/BF00117978 (Publisher: Kluwer Academic Publishers) doi: 10.1007/BF00117978

Mahrt, L. (2011, September). The Near-Calm Stable Boundary Layer. *Boundary-Layer Meteorology*, *140*(3), 343–360. Retrieved 2020-07-26, from http://link.springer.com/10.1007/s10546-011-9616-2 doi: 10.1007/s10546-011-9616-2

Mahrt, L. (2014, January). Stably Stratified Atmospheric Boundary Layers. *Annual Review of Fluid Mechanics*, *46*(1), 23–45. Retrieved 2020-07-26, from http://www.annualreviews.org/doi/10.1146/annurev-fluid-010313-141354 doi: 10.1146/annurev-fluid-010313-141354

Mahrt, L., & Bou-Zeid, E. (2020, June). Non-stationary Boundary Layers. *Boundary-Layer Meteorology*. Retrieved 2020-07-26, from http://link.springer.com/10.1007/s10546-020-00533-w doi: 10.1007/s10546-020-00533-w

Maroneze, R., Acevedo, O. C., Costa, F. D., & Sun, J. (2019). Simulating the regime transition of the stable boundary layer using different simplified models. *Boundary-Layer Meteorology*, *170*(2), 305–321. (Publisher: Springer)

Mauritsen, T., Svensson, G., Zilitinkevich, S. S., Esau, I., Enger, L., & Grisogono, B. (2007, November). A Total Turbulent Energy Closure Model for Neutrally and Stably Stratified Atmospheric Boundary Layers. *Journal of Atmospheric Sciences*, *64*(11), 4113–4126. Retrieved from http://journals.ametsoc.org/doi/10.1175/2007JAS2294.1 doi: 10.1175/2007JAS2294.1

Parente, A., Gorlé, C., van Beeck, J., & Benocci, C. (2011, September). A Comprehensive Modelling Approach for the Neutral Atmospheric Boundary Layer: Consistent Inflow Conditions, Wall Function and Turbulence Model. *Boundary-Layer Meteorology*, *140*(3), 411–428. Retrieved 2021-02-10, from http://link.springer.com/10.1007/s10546-011-9621-5 doi: 10.1007/s10546-011-9621-5

Rodrigo, J. S., & Anderson, P. S. (2013, September). Investigation of the Stable Atmospheric Boundary Layer at Halley Antarctica. *Boundary-Layer Meteorology*, *148*(3), 517–539. Retrieved 2020-10-14, from http://link.springer.com/10.1007/s10546-013-9831-0 doi: 10.1007/s10546-013-9831-0

Sandu, I., Beljaars, A., Bechtold, P., Mauritsen, T., & Balsamo, G. (2013, June). Why is it so difficult to represent stably stratified conditions in numerical weather prediction (NWP) models? *Journal of Advances in Modeling Earth Systems*, *5*(2), 117–133. Retrieved 2020-07-26, from http://doi.wiley.com/10.1002/jame.20013 doi: 10.1002/jame.20013

Sanz Rodrigo, J., Churchfield, M., & Kosovic, B. (2017, February). A methodology for the design and testing of atmospheric boundary layer models for wind energy applications. *Wind Energy Science*, *2*(1), 35–54. Retrieved 2021-05-09, from https://wes.copernicus.org/articles/2/35/2017/ doi: 10.5194/wes-2-35-2017

Scott, D. W. (2015). *Multivariate Density Estimation.* Wiley. Retrieved from https://doi.org/10.1002/9781118575574 doi: 10.1002/9781118575574

Sorbjan, Z. (2012). A study of the stable boundary layer based on a single-column

K-theory model. *Boundary-layer meteorology*, *142*(1), 33–53. (Publisher: Springer)

Steeneveld, G.-J., Nappo, C. J., & Holtslag, A. A. (2009, December). Estimation of orographically induced wave drag in the stable boundary layer during the CASES-99 experimental campaign. *Acta Geophysica*, *57*(4), 857–881. Retrieved 2023-05-11, from `https://doi.org/10.2478/s11600-009-0028-3` doi: 10.2478/s11600-009-0028-3

Stull, R. B. (1988). *An introduction to boundary layer meteorology* (Vol. 13). Springer Science & Business Media.

Sukoriansky, S., Galperin, B., & Staroselsky, I. (2005). A quasinormal scale elimination model of turbulent flows with stable stratification. *Physics of Fluids*, *17*(8), 085107. Retrieved from `http://link.aip.org/link/PHFLE6/v17/i8/p085107/s1&Agg=doi` doi: 10.1063/1.2009010

Sun, J., Burns, S. P., Lenschow, D. H., Banta, R., Newsom, R., Coulter, R., … Hu, X.-Z. (2002, November). Intermittent Turbulence Associated with a Density Current Passage in the Stable Boundary Layer. *Boundary-Layer Meteorology*, *105*(2), 199–219. Retrieved 2021-08-10, from `http://link.springer.com/10.1023/A:1019969131774` doi: 10.1023/A:1019969131774

Tjernström, M., Žagar, M., Svensson, G., Cassano, J. J., Pfeifer, S., Rinke, A., … Shaw, M. (2005, November). Modelling the Arctic Boundary Layer: An Evaluation of Six Arcmip Regional-Scale Models using Data from the Sheba Project. *Boundary-Layer Meteorology*, *117*(2), 337–381. Retrieved 2023-02-07, from `https://doi.org/10.1007/s10546-004-7954-z` doi: 10.1007/s10546-004-7954-z

van de Wiel, B. J. H., & Moene, A. F. (2003). Intermittent turbulence in the stable boundary layer over land. Part III: A classification for observations during CASES-99. *Journal of Atmospheric Sciences*, *60*(20), 2509–2522. Retrieved from `http://journals.ametsoc.org/doi/pdf/10.1175/1520-0469(2003)060%3C2509%3AITITSB%3E2.0.CO%3B2`

Van de Wiel, B. J. H., Moene, A. F., Jonker, H. J. J., Baas, P., Basu, S., Donda, J. M. M., … Holtslag, A. A. M. (2012, November). The Minimum Wind Speed for Sustainable Turbulence in the Nocturnal Boundary Layer. *Journal of the Atmospheric Sciences*, *69*(11), 3116–3127. Retrieved 2021-11-15, from `https://journals.ametsoc.org/doi/10.1175/JAS-D-12-0107.1` doi: 10.1175/JAS-D-12-0107.1

Van de Wiel, B. J. H., Vignon, E., Baas, P., van Hooijdonk, I. G. S., van der Linden, S. J. A., Antoon van Hooft, J., … Genthon, C. (2017, April). Regime Transitions in Near-Surface Temperature Inversions: A Conceptual Model. *Journal of the Atmospheric Sciences*, *74*(4), 1057–1073. Retrieved 2020-07-26, from `https://journals.ametsoc.org/jas/article/74/4/1057/342605/Regime-Transitions-in-NearSurface-Temperature` doi: 10.1175/JAS-D-16-0180.1

Vercauteren, N., Mahrt, L., & Klein, R. (2016, July). Investigation of interactions between scales of motion in the stable boundary layer: Interactions between Scales of Motion in the Stable Boundary Layer. *Quarterly Journal of the Royal Meteorological Society*, *142*(699), 2424–2433. Retrieved 2020-07-26, from `http://doi.wiley.com/10.1002/qj.2835` doi: 10.1002/qj.2835

Želi, V., Brethouwer, G., Wallin, S., & Johansson, A. V. (2019). Consistent boundary-condition treatment for computation of the atmospheric boundary layer using the explicit algebraic reynolds-stress model. *Boundary-Layer Meteorology*, *171*(1), 53–77. (Publisher: Springer)

Zilitinkevich, S. S., Elperin, T., Kleeorin, N., & Rogachevskii, I. (2007, September). Energy- and flux-budget (EFB) turbulence closure model for stably stratified flows. Part I: steady-state, homogeneous regimes. *Boundary-Layer Meteorology*, *125*(2), 167–191. Retrieved 2021-09-05, from `http://link.springer`

.com/10.1007/s10546-007-9189-2 doi: 10.1007/s10546-007-9189-2

Figure 1.

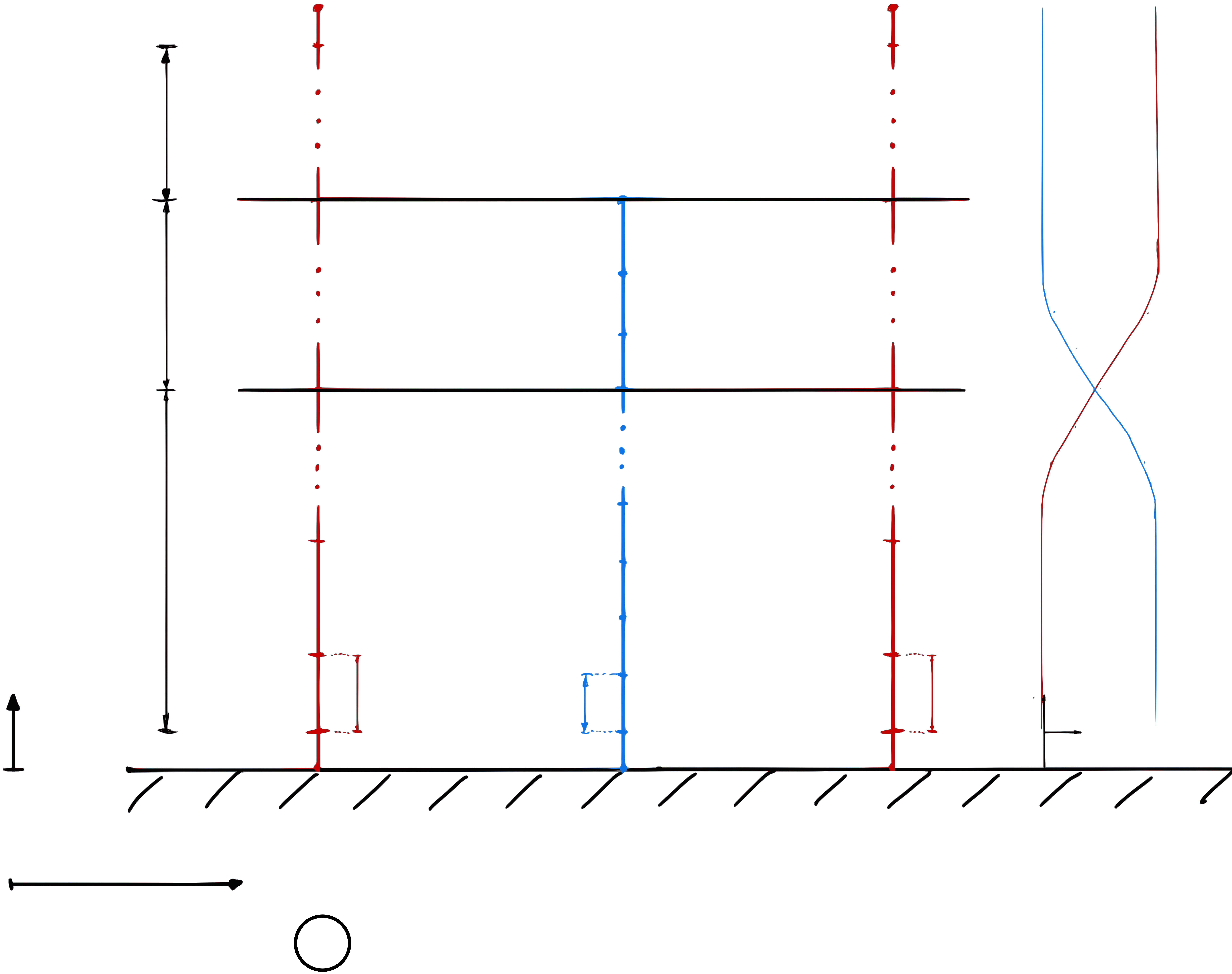

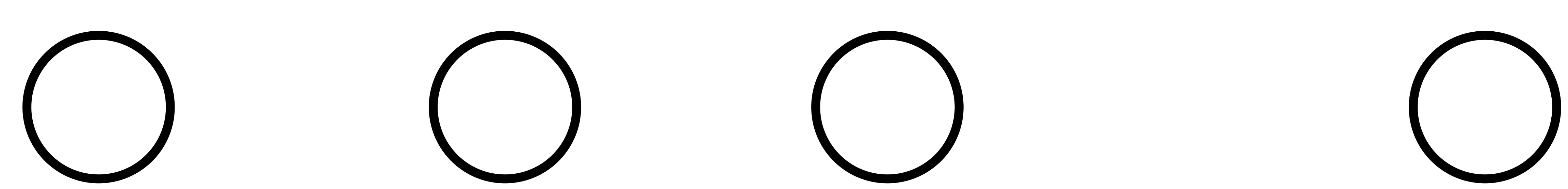

Figure 2.

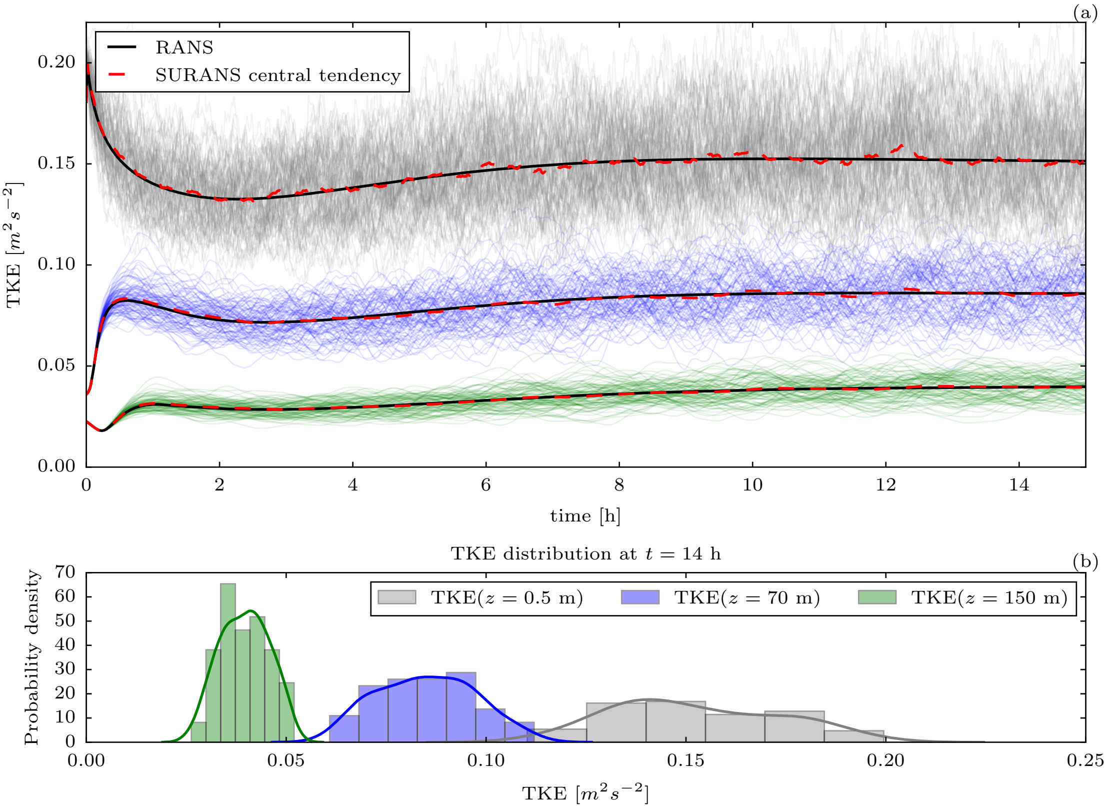

(a)
RANS
SURANS central tendency
TKE $[m^2s^{-2}]$
0.00
0.05
0.10
0.15
0.20
time [h]
0
2
4
6
8
10
12
14
TKE distribution at $t = 14$ h
(b)
TKE($z = 0.5$ m)
TKE($z = 70$ m)
TKE($z = 150$ m)
Probability density
0
10
20
30
40
50
60
70
0.00
0.05
0.10
0.15
0.20
0.25
TKE $[m^2s^{-2}]$

Figure 3.

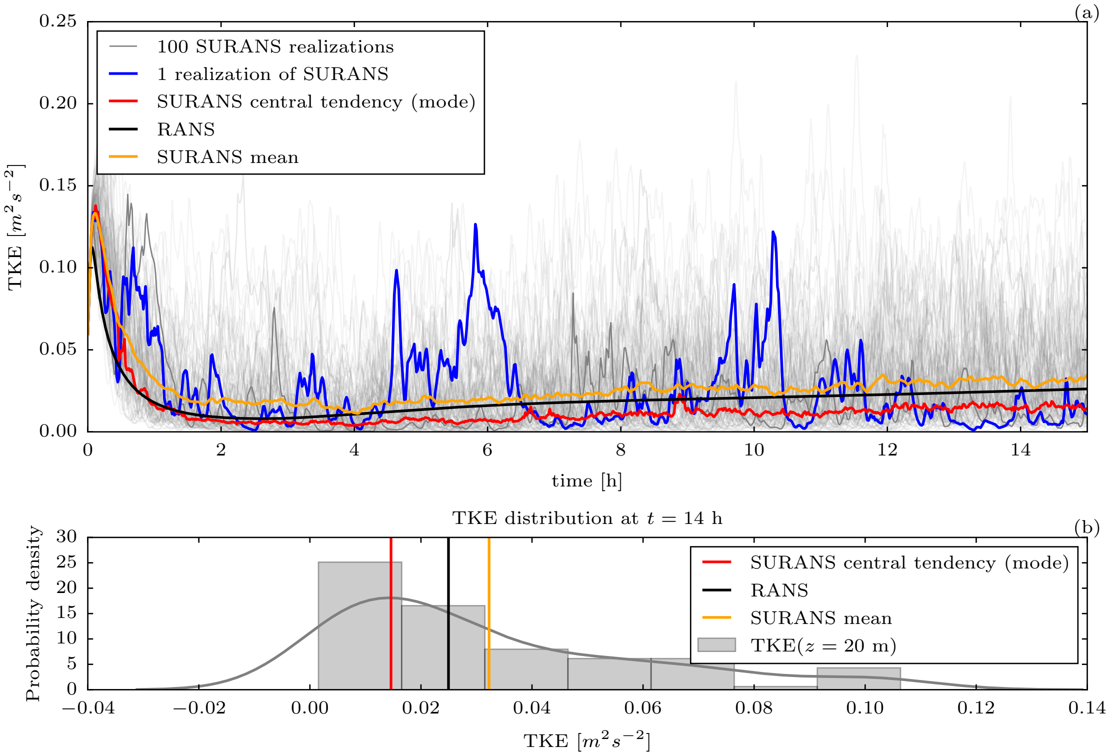
(a)
100 SURANS realizations
1 realization of SURANS
SURANS central tendency (mode)
RANS
SURANS mean
TKE $[m^2 s^{-2}]$
0.25
0.20
0.15
0.10
0.05
0.00
0
2
4
6
8
10
12
14
time [h]
TKE distribution at $t = 14$ h
(b)
Probability density
30
25
20
15
10
5
0
SURANS central tendency (mode)
RANS
SURANS mean
TKE($z = 20$ m)
−0.04
−0.02
0.00
0.02
0.04
0.06
0.08
0.10
0.12
0.14
TKE $[m^2 s^{-2}]$

Figure 4.

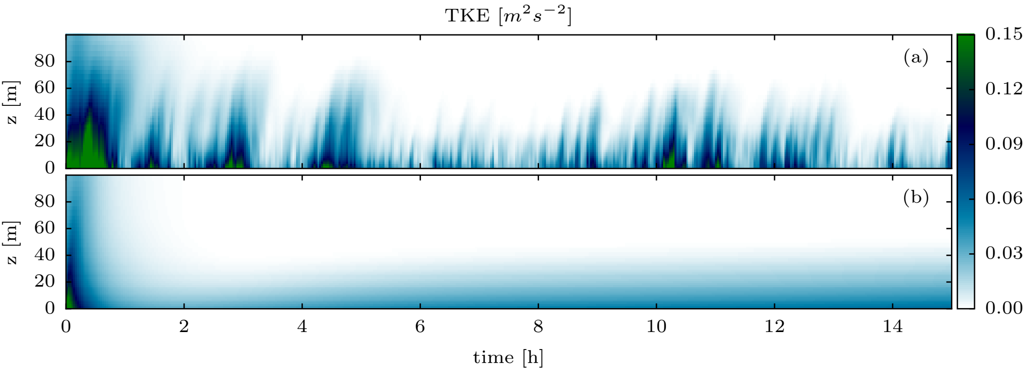
TKE $[m^2s^{-2}]$
(a)
(b)
z [m]
z [m]
0
20
40
60
80
0
20
40
60
80
0
2
4
6
8
10
12
14
time [h]
0.15
0.12
0.09
0.06
0.03
0.00

Figure 5.

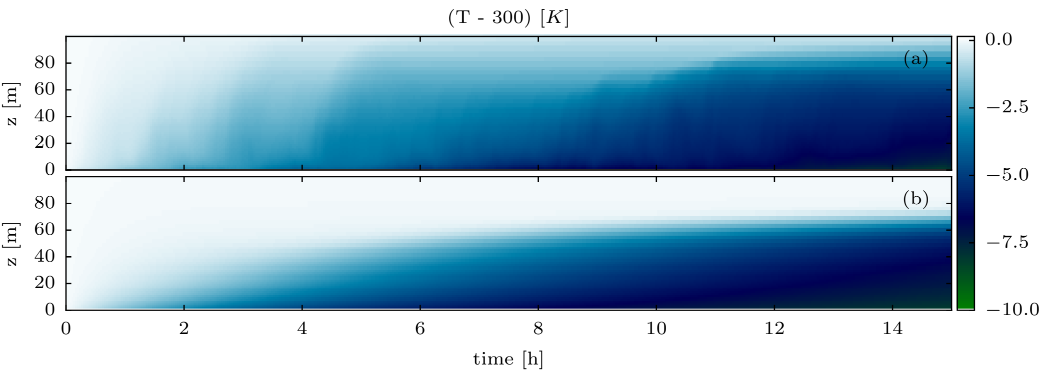

(T - 300) [K]
(a)
(b)
z [m]
0
20
40
60
80
time [h]
0
2
4
6
8
10
12
14
0.0
−2.5
−5.0
−7.5
−10.0

Figure 6.

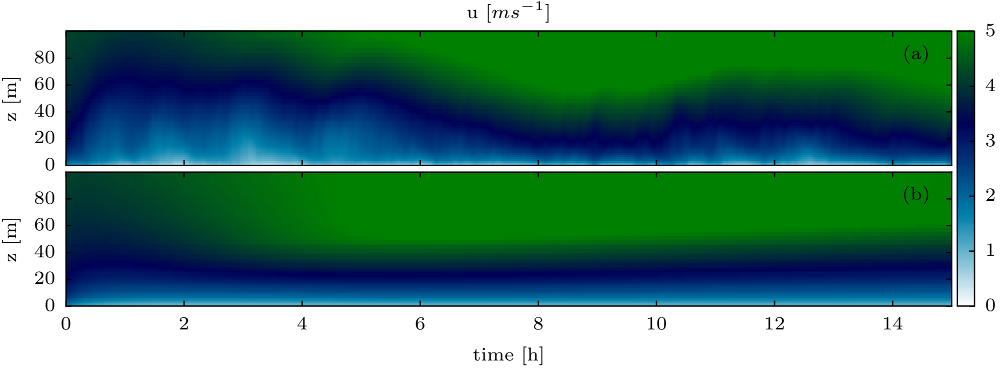

u $[ms^{-1}]$
(a)
(b)
z [m]
z [m]
0
20
40
60
80
0
20
40
60
80
0
2
4
6
8
10
12
14
time [h]
0
1
2
3
4
5

Figure 7.

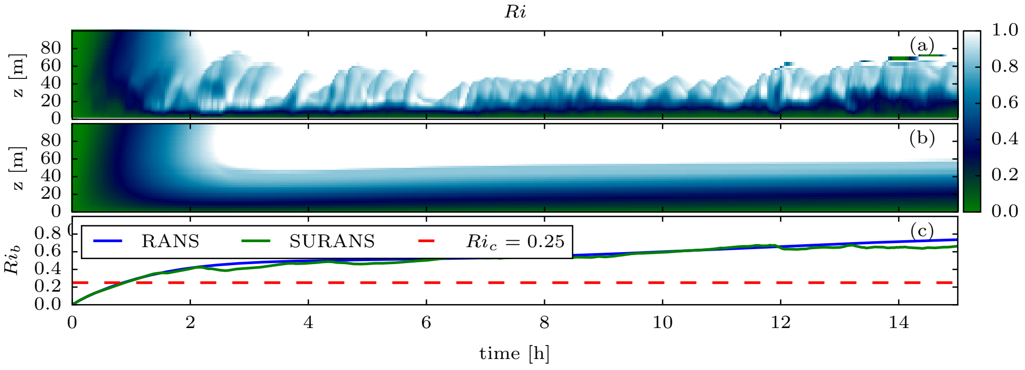

Ri
(a)
(b)
(c)
z [m]
z [m]
Ri_b
RANS
SURANS
$Ri_c = 0.25$
time [h]
0
2
4
6
8
10
12
14
0
20
40
60
80
0.0
0.2
0.4
0.6
0.8
1.0

Figure 8.

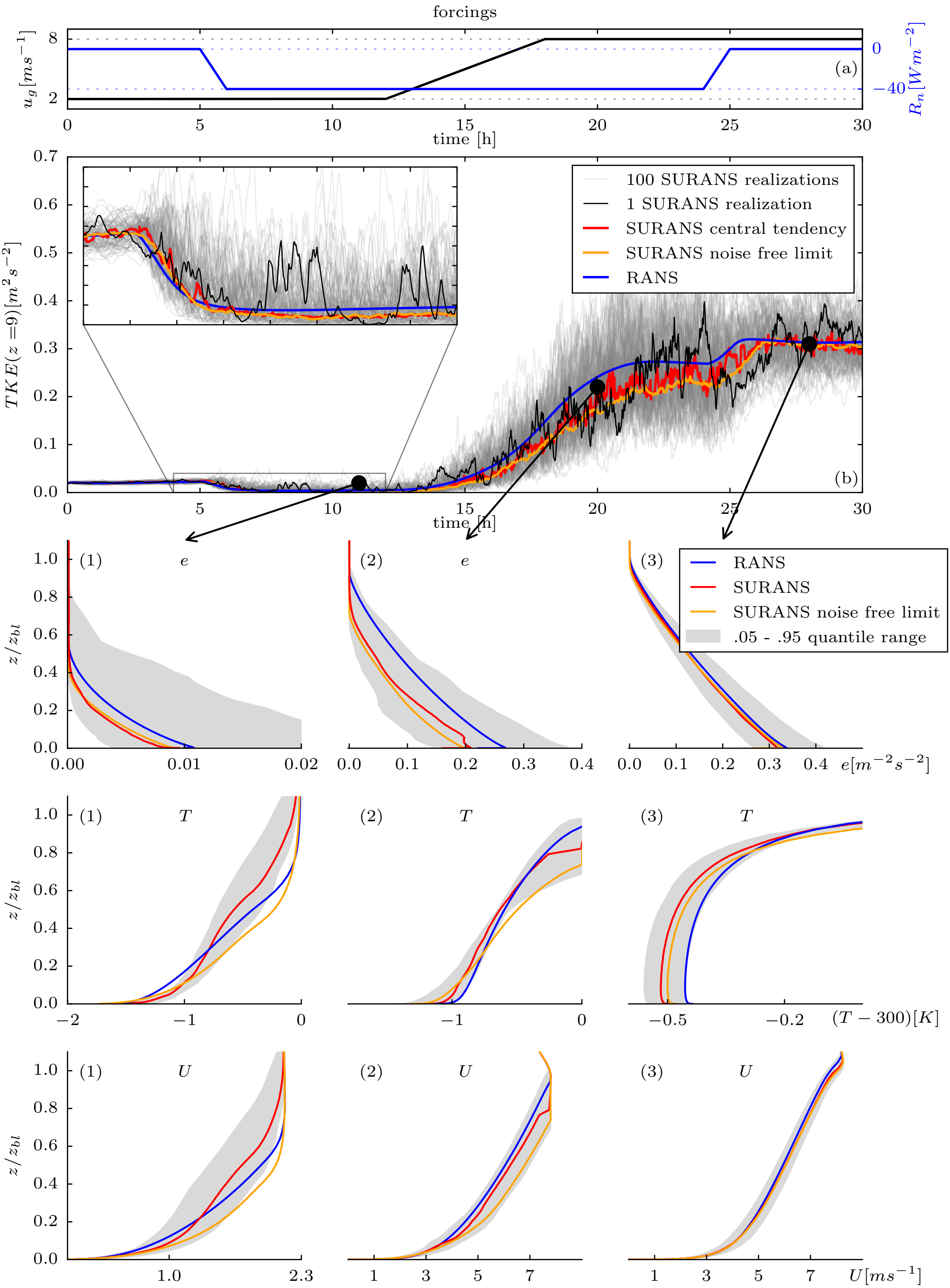

forcings
$u_g[ms^{-1}]$
$R_n[Wm^{-2}]$
(a)
time [h]
100 SURANS realizations
1 SURANS realization
SURANS central tendency
SURANS noise free limit
RANS
$TKE(z=9)[m^2s^{-2}]$
(b)
time [h]
(1) e
(2) e
(3)
RANS
SURANS
SURANS noise free limit
.05 - .95 quantile range
z/z_{bl}
$e[m^{-2}s^{-2}]$
(1) T
(2) T
(3) T
$(T-300)[K]$
(1) U
(2) U
(3) U
$U[ms^{-1}]$

Figure 9.

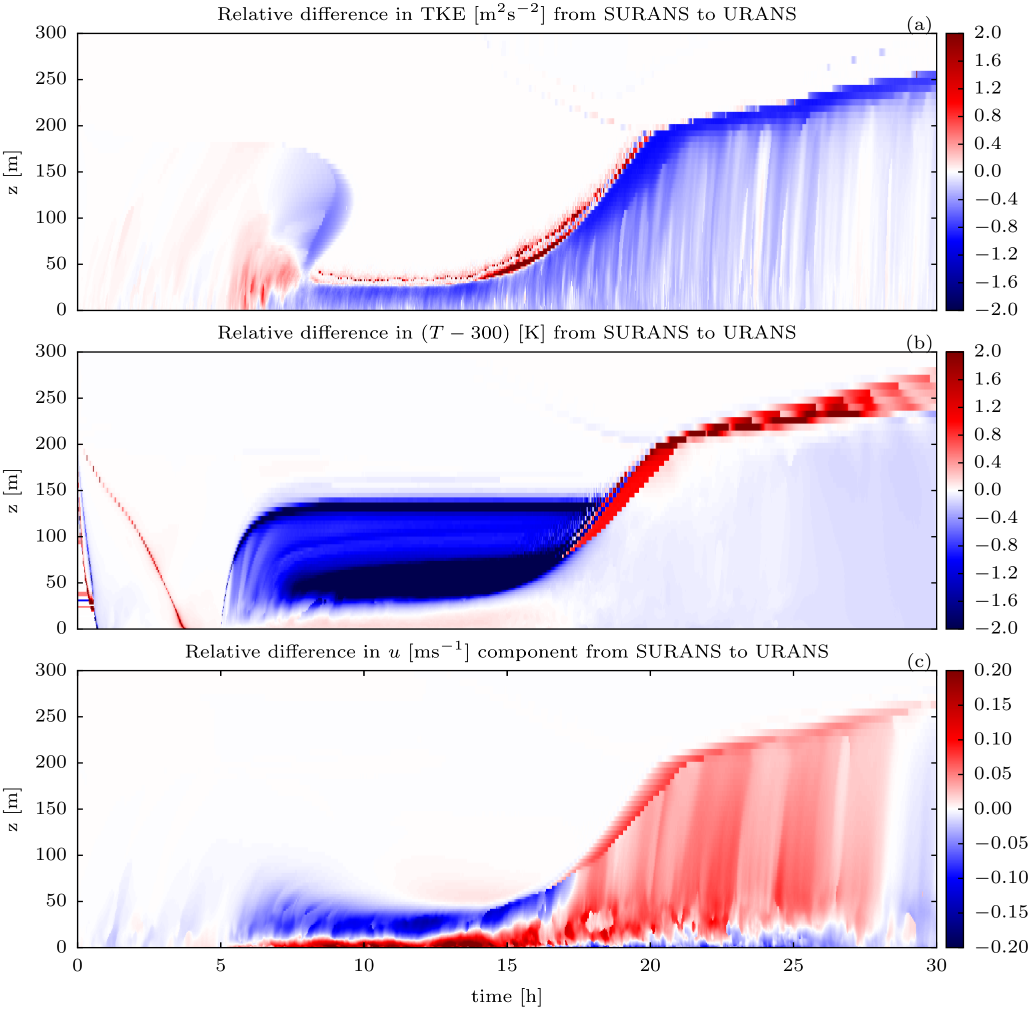

Relative difference in TKE $[m^2s^{-2}]$ from SURANS to URANS
(a)
Relative difference in $(T-300)$ [K] from SURANS to URANS
(b)
Relative difference in u $[ms^{-1}]$ component from SURANS to URANS
(c)
z [m]
time [h]
0
5
10
15
20
25
30
0
50
100
150
200
250
300
2.0
1.6
1.2
0.8
0.4
0.0
−0.4
−0.8
−1.2
−1.6
−2.0
0.20
0.15
0.10
0.05
0.00
−0.05
−0.10
−0.15
−0.20